Supporting Information for the paper:

Intercluster reactions between $Au_{25}(SR)_{18}$ and $Ag_{44}(SR)_{30}$

K. R. Krishnadas, Atanu Ghosh, Ananya Baksi, Indranath Chakraborty[†], Ganapati Natarajan and Thalappil Pradeep*

DST Unit of Nanoscience (DST UNS) and Thematic Unit of Excellence, Department of Chemistry, Indian Institute of Technology Madras, Chennai 600 036, India

[†]Currently a postdoctoral fellow at Dept. of Chemistry, University of Illinois at Urbana Champaign

*Email: pradeep@iitm.ac.in

Table of Contents

Instrumentation

Matrix assisted laser desorption ionization mass spectrometric (MALDI MS) studies were conducted using a Voyager DE PRO Biospectrometry Workstation (Applied Biosystems) matrix assisted laser desorption ionization time-of-flight mass spectrometer (MALDI TOF MS). Spectrometer was operated in the linear mode. The UV/Vis spectra were recorded using a Perkin Elmer Lambda 25 UV/Vis spectrometer. Absorption spectra were typically measured in the range of 200-1100 nm. Luminescence measurements were carried out on a JobinYvonNanoLog instrument.

ESI MS measurements

Waters Synapt G2-Si High Definition Mass Spectrometer equipped with Electrospray ionization, matrix assisted laser desorption ionization and ion mobility separation was used. All the samples were analyzed in negative mode electrospray ionization. The instrumental parameters were first

optimized for $Au_{25}(PET)_{18}$ and other samples were analyzed using the similar setting with slight modification depending on the sample. About 0.1 mg of as prepared samples were diluted dichloromethane (DCM) and directly infused to the system without any further purification. The instrument was calibrated using NaI as calibrant. The optimized conditions were as follows:

Sample concentration: 0.1 mg/mL
Diluents: DCM
Sample flow rate: 10-20 µL/min
Source Voltage: 2.5-3 kV
Cone Voltage: 120-140 V
Source Offset: 80-120 V
Trap Collision Energy: 0-20 V (For higher $Ag_{44}(FTP)_{30}$ concentration)
Transfer Collision Energy: 0-2 V
Source Temperature: 80-100°C
Desolvation Temperature: 150-200°C
Desolvation Gas Flow: 400 L/h

For fragmentation of $Au_{25}(PET)_{18}$, the molecular ion peak was first mass selected in the quadruple which is situated before T-wave region. Collision induced dissociation was performed in the first T-wave region (trap) and analyzed in the TOF region. A nominal collision energy of 80-120 V was used for the CID experiments. Below 50 V, $Au_{25}(PET)_{18}$ did not show any considerable fragmentation. Similar fragmentation was observed when the same sample was fragmented in-source without any mass selection.

$Ag_{44}(FTP)_{30}$ clusters were analyzed in DCM medium as the reaction was carried out in pure DCM. The experimental parameters optimized for $Ag_{44}(FTP)_{30}$are as follows:

Sample concentration: 0.05 mg/mL
Diluents: DCM
Sample flow rate: 10 µL/min
Source Voltage: 0.3-1.5 kV
Cone Voltage: 20-60 V
Source Offset: 30-40 V
Trap Collision Energy: 0-4 V
Transfer Collision Energy: 0-2 V
Source Temperature: 80°C
Desolvation Temperature: 150°C
Desolvation Gas Flow: 400 L/h

MALDI MS measurements: The matrix used was trans-2-[3-(4-tertbutylphenyl)-2-methyl-2-propenylidene]malononitrile (DCTB, > 98%). A solution of 6.2 mg of DCTB in 0.5 mL of dicholoromethane was used for the measurements. Appropriate volumes of the sample solutions and DCTB solutions in DCM were mixed thorougly and spotted on the sample plate and allowed to dry at ambient conditions. All the MALDI MS measurements were carried out at the threshold laser fluenece in order to minimize fragmentation. All the spectra reported are of negative ions. An average of 100 shots were taken for each mass spectrum.

Synthesis of $Na_4[Ag_{44}(MBA)_{30}]$: Initially 128 mg of $AgNO_3$ was added to a mixture of DMSO and water (4:7 volume ratio) in a beaker under constant stirring. About 173 mg of MBA was then added to the mixture while stirring. This results in the formation of thiolates which gives a cloudy appearance to the solution. About 50% CsOH was then added drop wise till the solution was clear and a greenish yellow color appeared. After this, $NaBH_4$ solution (283 mg in 9 mL water) was added dropwise. Slowly the color changes to deep brown and after 1 h the color becomes deep red indicating the formation of clusters. This crude cluster solution was purified by precipitating it by the addition of DMF. The precipitate was collected by centrifugation. The centrifugate was then removed and the cluster was extracted in citric acid containing DMF. Role of citric acid is to acidify all the protons of carboxylic acid groups of MBA ligand which will make the cluster soluble in DMF. The resultant cluster solution was then again precipitated using toluene and centrifuged. The acidification step was repeated one more time. After this, the precipitate was redissolved in DMF to get the purified cluster.

Computational Details: The $Ag(4d^{10}5s^1)$, $Au(5d^{10}6s^1)$, and $S(3s^23p^4)$ electrons were treated as valence and the inner electrons were included in a frozen core. The GPAW setups[1] for gold and silver included scalar-relativistic corrections. The exchange-correlation functional employed was the generalized gradient approximation of Perdew, Burke and Ernzerhof (GGA-PBE).[2] We used a 0.2Å grid spacing for electron density in all calculations and a convergence criterion of 0.05 eV/Å for the residual forces on atoms was used in all structure optimizations, without any symmetry constraints. For computational efficiency during the structural optimizations, rather than employing the finite-difference real-space grid method for the expansion of the pseudowavefunctions, we used instead the LCAO method[3] as implemented in GPAW by employing a double zeta plus polarization (DZP) basis set. For greater precision in our reaction energy calculations, we then recalculated the total energies at this geometry minimum using the finite-difference method in GPAW. The crystal structures of $Au_{25}(SR)_{18}$[4] and $Ag_{44}(SR)_{30}$[5] were used for the initial structures of the calculations. For efficient computations, we terminated each sulfur atom with a hydrogen atom in all the clusters.

The initial structures of $[Au_{25}(SR)_{18}]^-$ and $[Ag_{44}(SR)_{30}]^{4-}$ were first geometry optimized, and then a single metal (Ag or Au) atom was replaced in a symmetry non-equivalent position and the geometries of the resulting $[Au_{24}Ag(SR)_{18}]^-$ and $[Au_{43}Au(SR)_{30}]^{4-}$ configurations were then optimized. The value of the total energy of each isomer was taken at the geometry-optimized configuration using the LCAO method but then recalculated using the more accurate finite-difference method in GPAW. We also computed the total energies of Au and Ag atoms using spin-polarization applying Hund's rule to the ground-state electronic configuration (of the isolated atoms) and the energies in the geometry-optimized configurations of AuSH and AgSH clusters in charge neutral states. The exchange reaction energies of Au(Ag) and Au(Ag)-SH into different positions in both of the clusters were calculated as E(Reaction) = E(Products) - E(Reactants)

The structures of $Au_{25}[PET]_{18}$ and $Ag_{44}[FTP]_{30}$ were built up with the help of Avogadro software package[6] and visualizations were created with Visual Molecular Dynamics (VMD)

software.[7] The structures have been modeled assuming coordinates from the crystal structures of $Au_{25}(SR)_{18}$[4] and $Ag_{44}(SR)_{30}$.[5]

Supporting Information 1

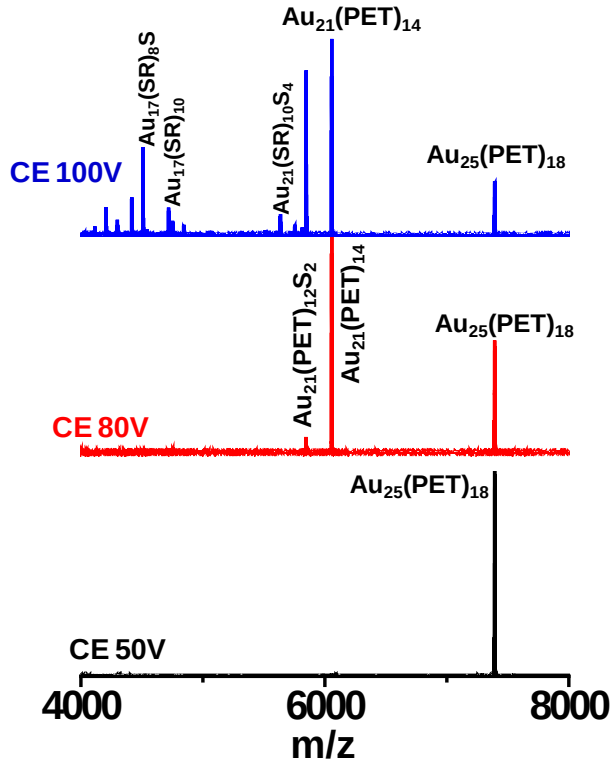

Figure S1. Collision energy-dependent ESI MS spectra of $Au_{25}(PET)_{18}$. Loss of $Au_4(SR)_4$ unit resulting in $Au_{21}(SR)_{14}$ is the typical fragmentation mode of $Au_{25}(SR)_{18}$.[8]

Supporting Information 2

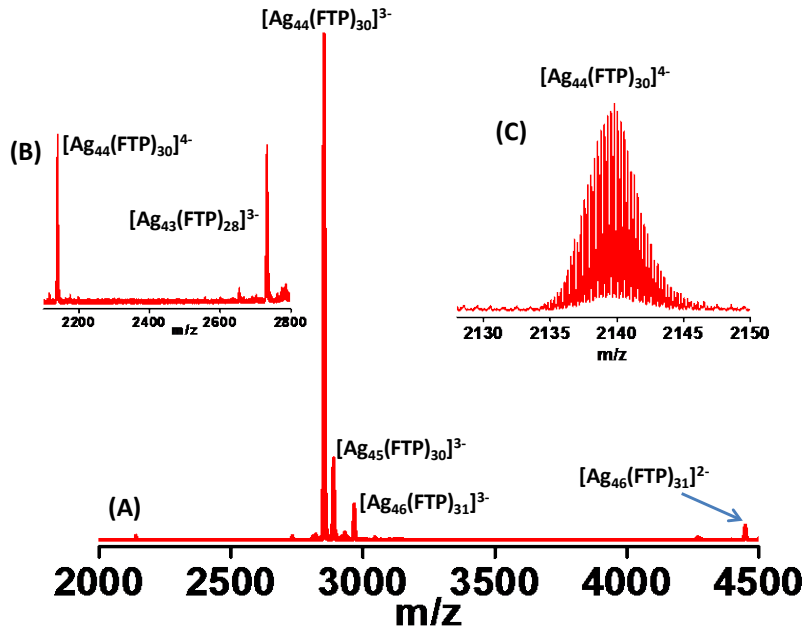

Figure S2. ESI MS spectrum of $Ag_{44}(FTP)_{30}$ shown in trace b' of Figure 1B. Lower m/z region in A is expanded in B to show the fragmentation of $[Ag_{44}(FTP)_{30}]^{4-}$ to give $[Ag_{43}(FTP)_{28}]^{3-}$. Such a fragmentation pattern is in accordance with previous reports (see Ref. 2e and 2g in main manuscript). Isotope distribution of $[Ag_{44}(FTP)_{30}]^{4-}$ is shown in C. Species such as $[Ag_{45}(FTP)_{30}]^{3-}$ and $[Ag_{46}(FTP)_{31}]^{3-}$ were also detected which could be due to minor byproducts.

Supporting Information 3

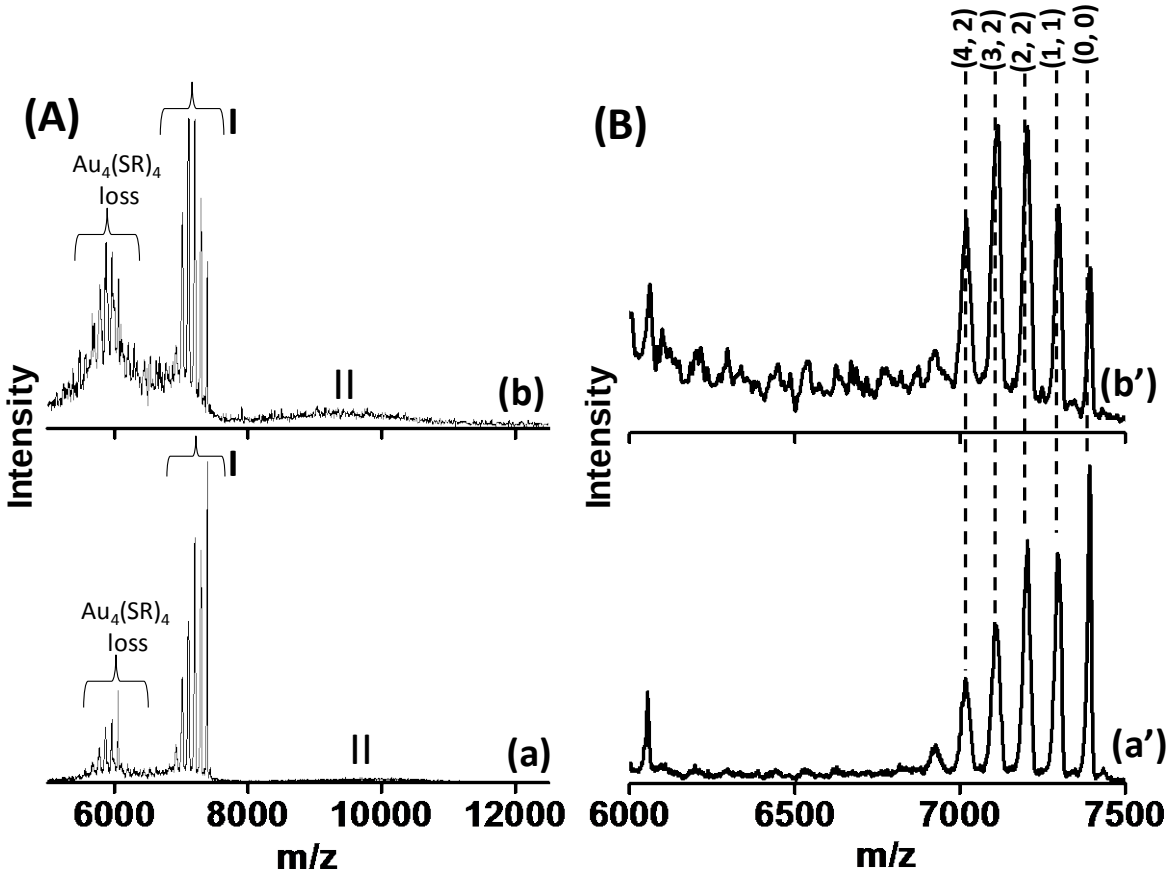

Figure S3. MALDI MS spectra showing the temporal evolution of the products formed after mixing of $Au_{25}(PET)_{18}$ and $Ag_{44}(FTP)_{30}$ clusters at Au_{25}:Ag_{44} ratio of 14:1. Traces a and b in (A) are the mass spectra of the reaction mixture immediately after mixing and after 1h of mixing, respectively. The group I in a and b are expanded in a' and b', respectively. The numbers in parentheses, (*x*, *y*), are according to the general molecular formula, $Au_{25-x}Ag_x(PET)_{18-y}(FTP)_y$. $Au_4(SR)_4$ loss is a standard fragementation pattern of $Au_{25}(SR)_{18}$ clusters (see Figure S1).

Supporting Information 4

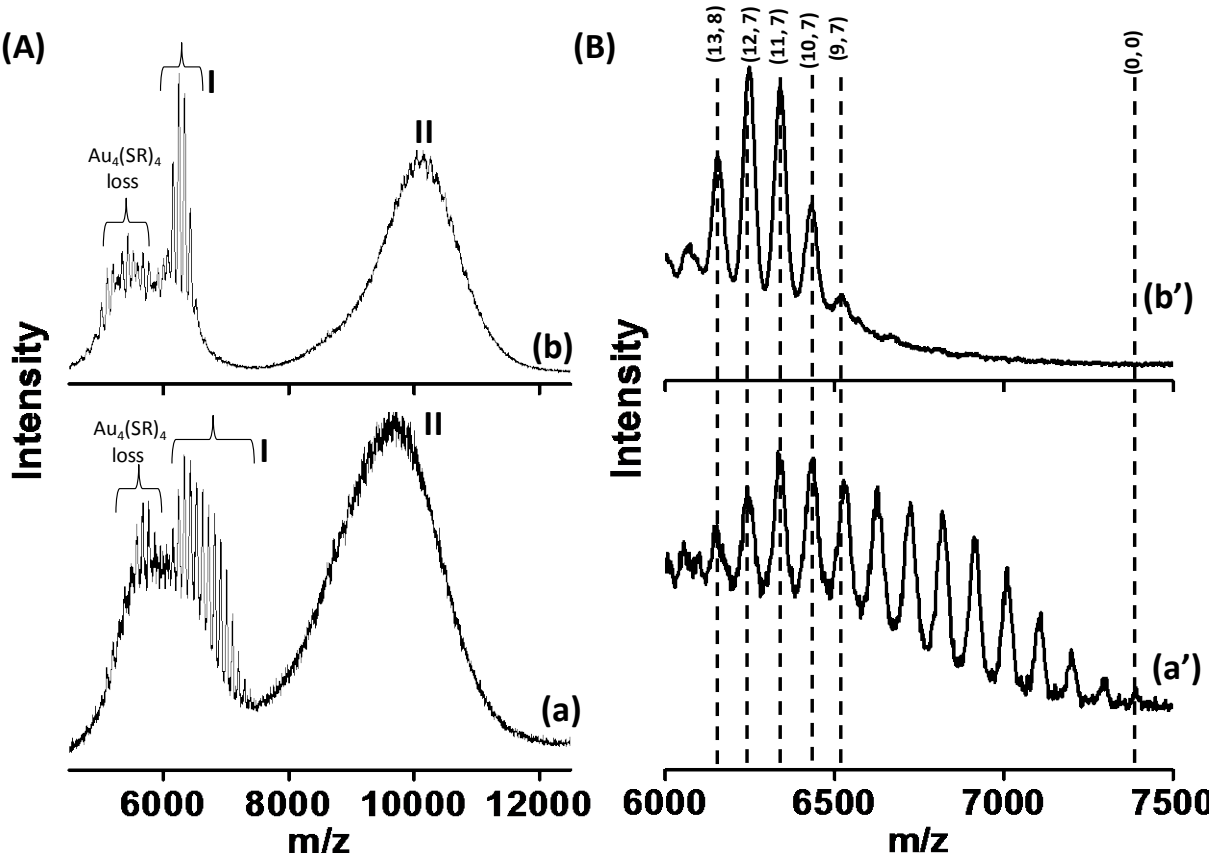

Figure S4. MALDI MS spectra showing the temporal evolution of the products formed after mixing of $Au_{25}(PET)_{18}$ and $Ag_{44}(FTP)_{30}$ clusters at Au_{25}:Ag_{44} ratio of 1.7:1. Traces a and b in (A) are the mass spectra of the reaction mixture immediately after mixing and after 1h of mixing, respectively. The group I in a and b are expanded in a' and b', respectively. The numbers in parentheses, (*x*, *y*), are according to the general molecular formula, $Au_{25-x}Ag_x(PET)_{18-y}(FTP)_y$. Au_4SR_4 loss is a standard fragementation pattern of $Au_{25}(SR)_{18}$ clusters (see Figure S1).

Supporting Information 5

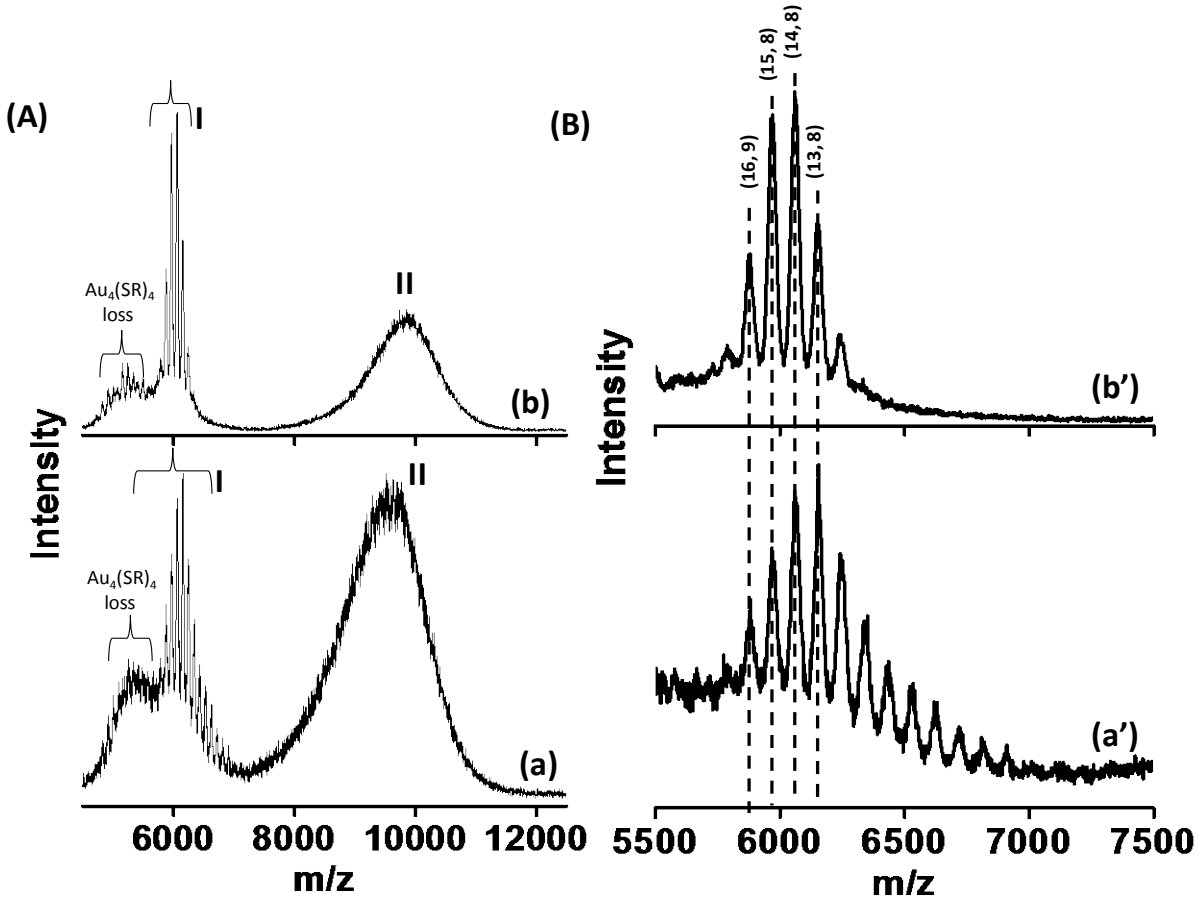

Figure S5. MALDI MS spectra showing the temporal evolution of the products formed after mixing of $Au_{25}(PET)_{18}$ and $Ag_{44}(FTP)_{30}$ clusters at Au_{25}:Ag_{44} ratio of 1.0:1.0. Traces a and b in (A) are the mass spectra of the reaction mixture immediately after mixing and after 1h of mixing, respectively. The group I in a and b are expanded in a' and b', respectively. The numbers in parenthesis, (x, y), are according to the general molecular formula, $Au_{25-x}Ag_x(PET)_{18-y}(FTP)_y$.

Note: In Figures S3, S4 and S14, peaks labels are assigned considering the peak maxima alone. However, ESI MS data (see Figure 3 insets, Figures S5-S9), shows that there are additional peaks in each of these features which is not resolved in MALDI MS due to the broadness of peaks.

Supporting Information 6

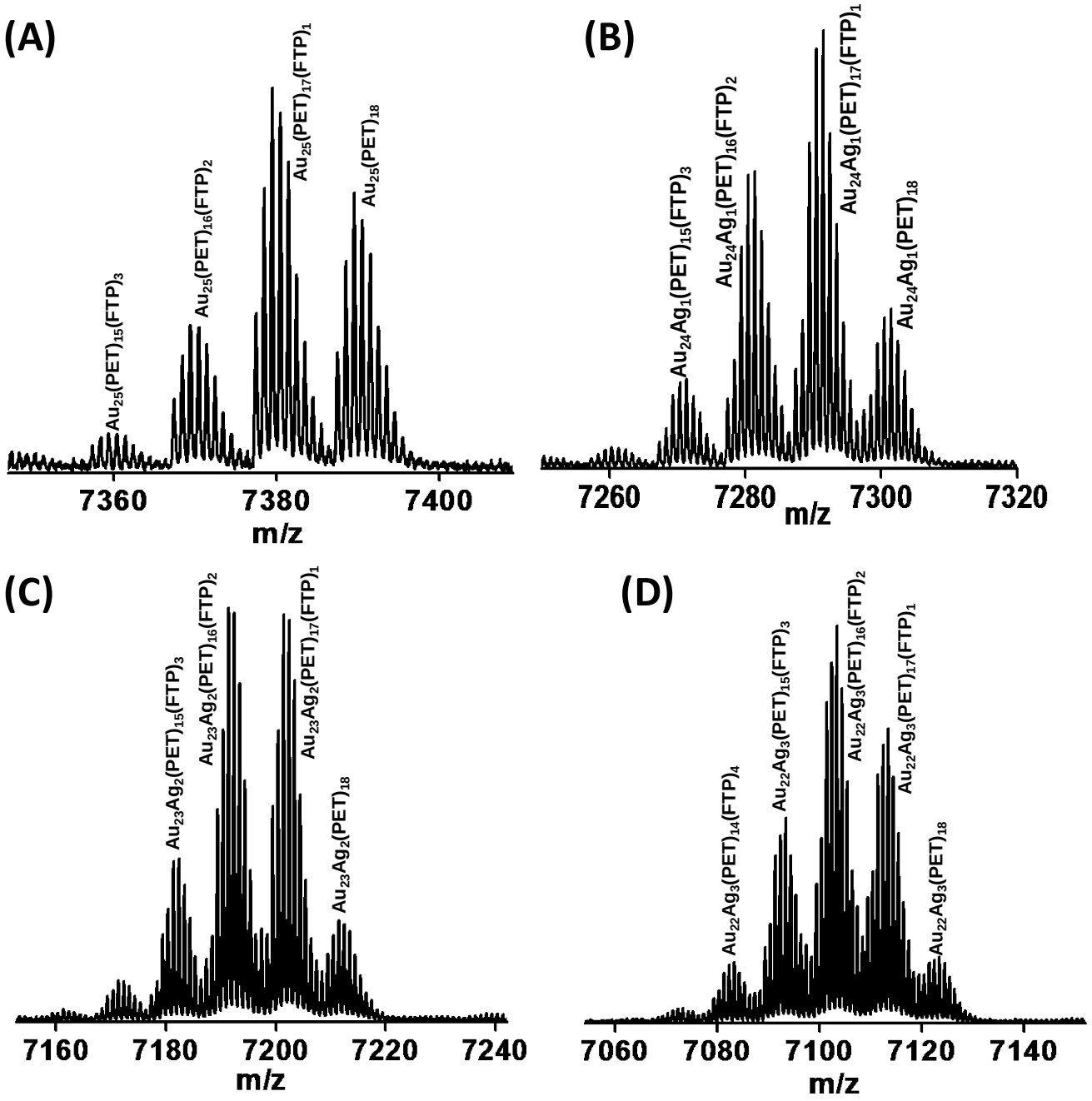

Figure S6. Panels A-D shows the expansion of features (0, 0-3), (1, 0-4), (2, 0-4) and (3, 0-4), (shown in Figure 3), respectively. The numbers, for example, (0, 0-3) is according to the general formula, $Au_{25-x}Ag_x(PET)_{18-y}(FTP)_y$.

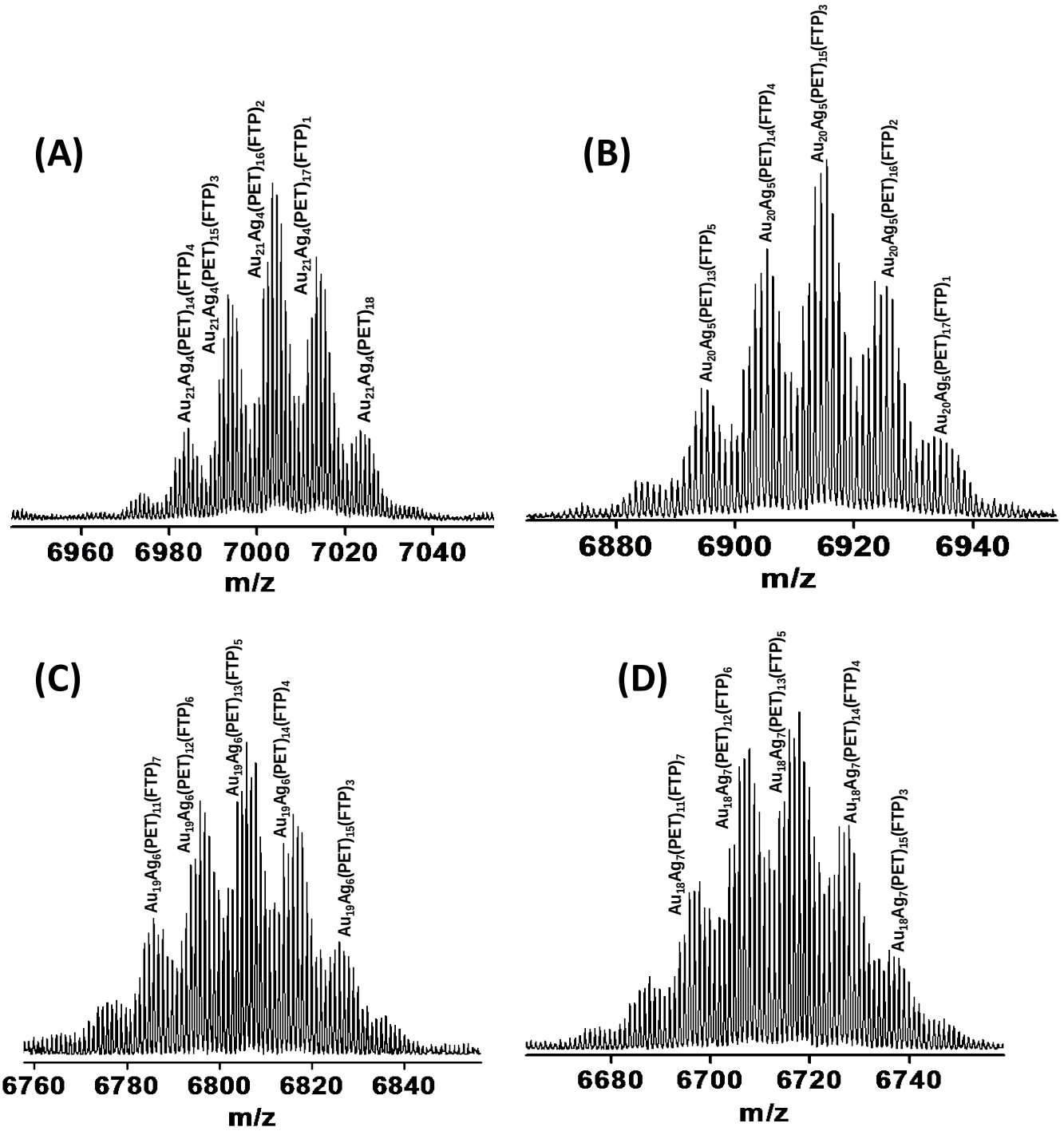

Figure S7. Panels A-D shows the expansion of features (4, 1-5), (5, 1-5), (6, 3-8) and (7, 3-8), (shown in Figure 3) respectively. The numbers, for example, (4, 1-5) is according to the general formula, $Au_{25-x}Ag_x(PET)_{18-y}(FTP)_y$.

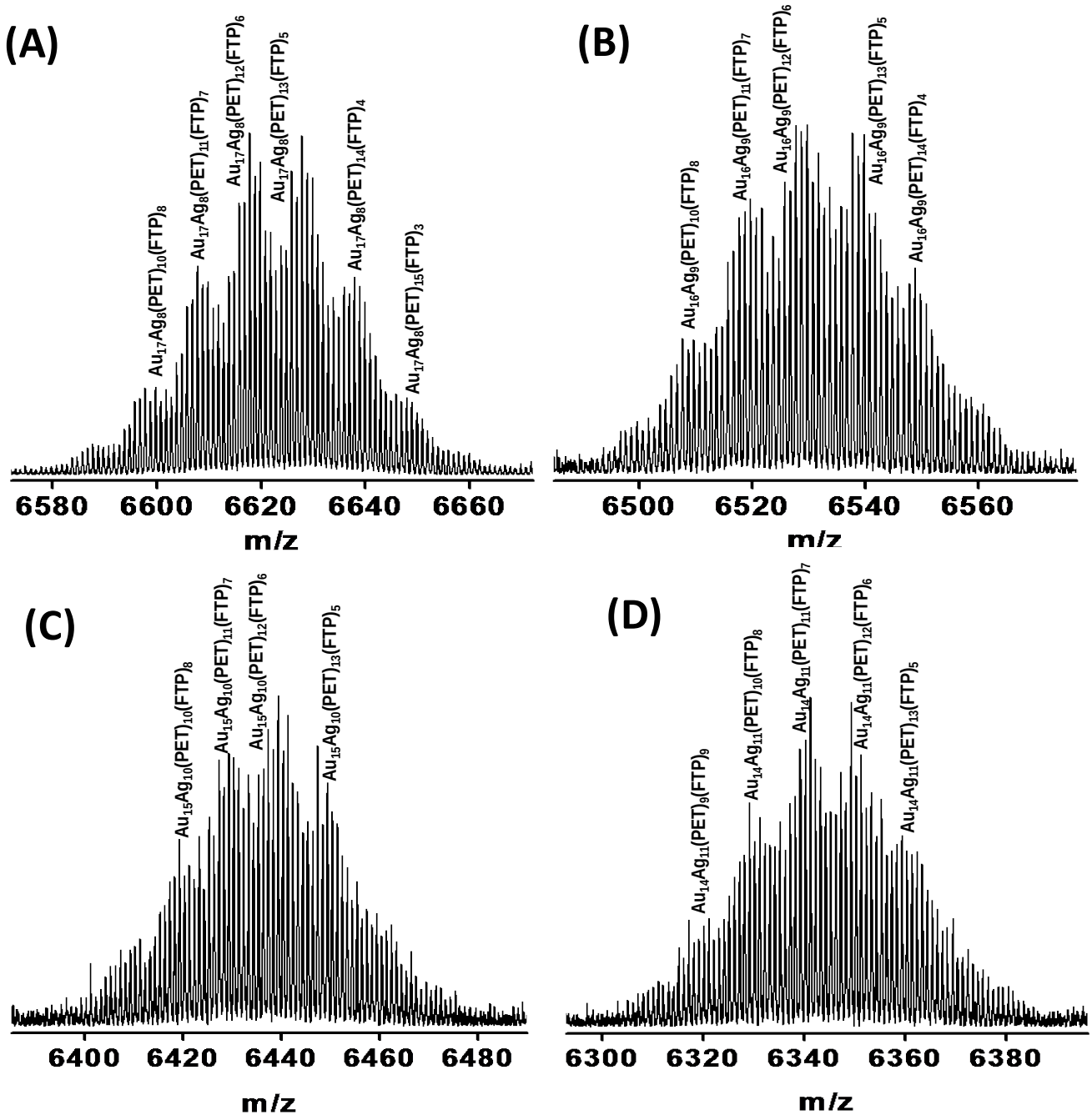
(A)
$Au_{17}Ag_8(PET)_{10}(FTP)_8$
$Au_{17}Ag_8(PET)_{11}(FTP)_7$
$Au_{17}Ag_8(PET)_{12}(FTP)_6$
$Au_{17}Ag_8(PET)_{13}(FTP)_5$
$Au_{17}Ag_8(PET)_{14}(FTP)_4$
$Au_{17}Ag_8(PET)_{15}(FTP)_3$
6580 6600 6620 6640 6660
m/z
(B)
$Au_{16}Ag_9(PET)_{10}(FTP)_8$
$Au_{16}Ag_9(PET)_{11}(FTP)_7$
$Au_{16}Ag_9(PET)_{12}(FTP)_6$
$Au_{16}Ag_9(PET)_{13}(FTP)_5$
$Au_{16}Ag_9(PET)_{14}(FTP)_4$
6500 6520 6540 6560
m/z
(C)
$Au_{15}Ag_{10}(PET)_{10}(FTP)_8$
$Au_{15}Ag_{10}(PET)_{11}(FTP)_7$
$Au_{15}Ag_{10}(PET)_{12}(FTP)_6$
$Au_{15}Ag_{10}(PET)_{13}(FTP)_5$
6400 6420 6440 6460 6480
m/z
(D)
$Au_{14}Ag_{11}(PET)_9(FTP)_9$
$Au_{14}Ag_{11}(PET)_{10}(FTP)_8$
$Au_{14}Ag_{11}(PET)_{11}(FTP)_7$
$Au_{14}Ag_{11}(PET)_{12}(FTP)_6$
$Au_{14}Ag_{11}(PET)_{13}(FTP)_5$
6300 6320 6340 6360 6380
m/z

Figure S8. Panels A-D shows the expansion of features (8, 3-9), (9, 3-9), (10, 4-9) and (11, 4-9), (shown in Figure 3) respectively. The numbers, for example, (8, 3-9) is according to the general formula, $Au_{25-x}Ag_x(PET)_{18-y}(FTP)_y$.

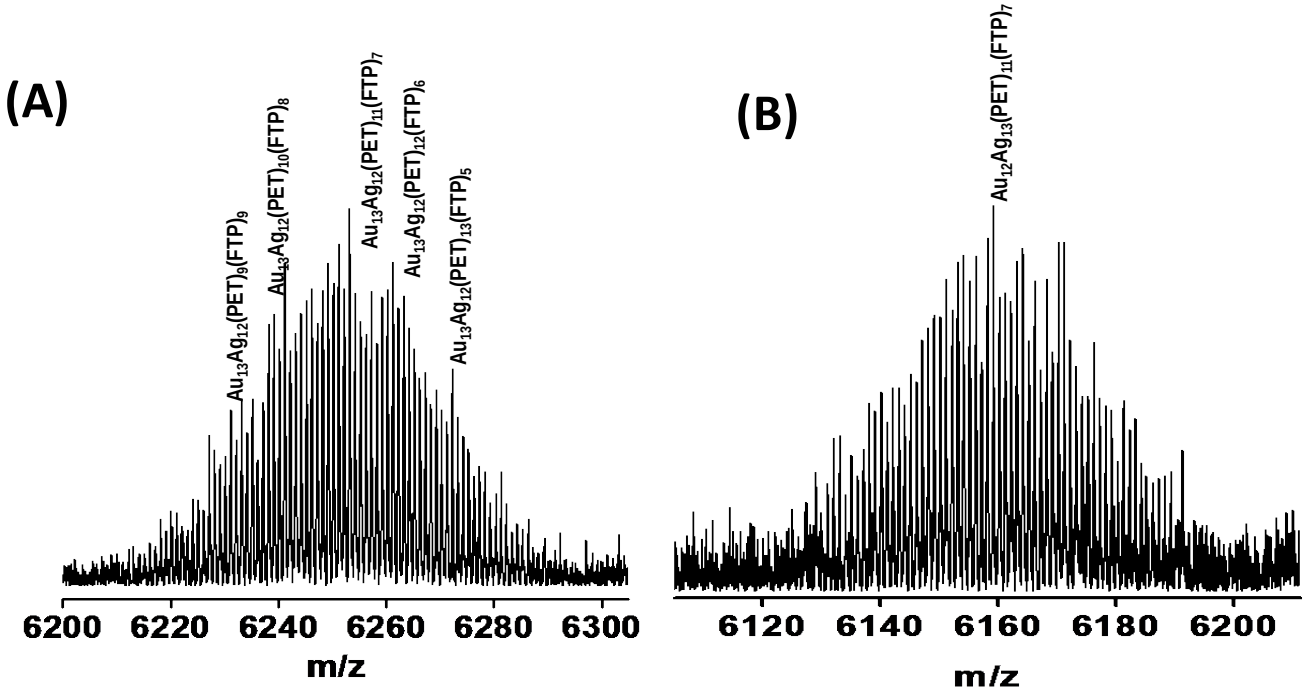

Figure S9. Panels A and B shows the expansion of features (12, 4-9) and (13, 4-9), (shown in Figure 3) respectively. The numbers, for example, (12, 4-9) is according to the general formula, $Au_{25-x}Ag_x(PET)_{18-y}(FTP)_y$.

Supporting Information 7

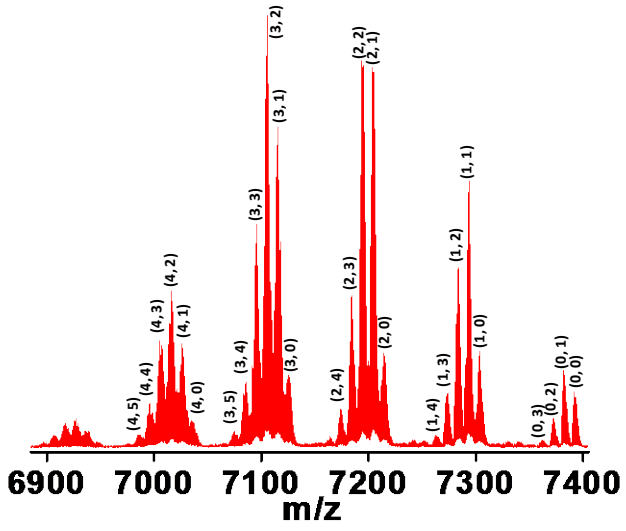

Figure S10. Expansion of the mass spectra in panel A of Figure 3 in the Article.

Supporting Information 8

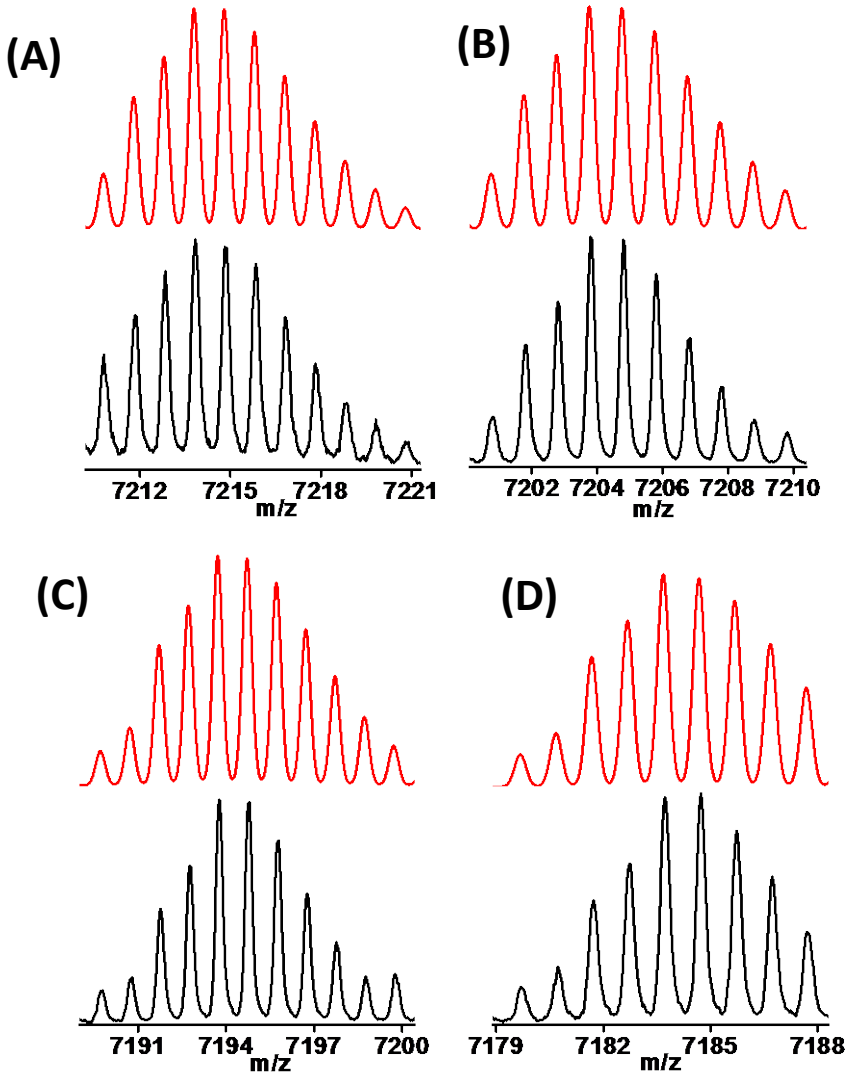

Figure S11. Experimental (black trace) and theoretical (red trace) isotope distributions of (A) $Au_{23}Ag_2(PET)_{18}$, (B) $Au_{23}Ag_2(PET)_{17}(FTP)_1$, (C) $Au_{23}Ag_2(PET)_{16}(FTP)_2$ and (D) $Au_{23}Ag_2(PET)_{15}(FTP)_3$. These species corresponds to those labeled as (2, 0), (2, 1), (2, 2) and (2, 3), respectively in Figure 3A inset.

Supporting Information 9

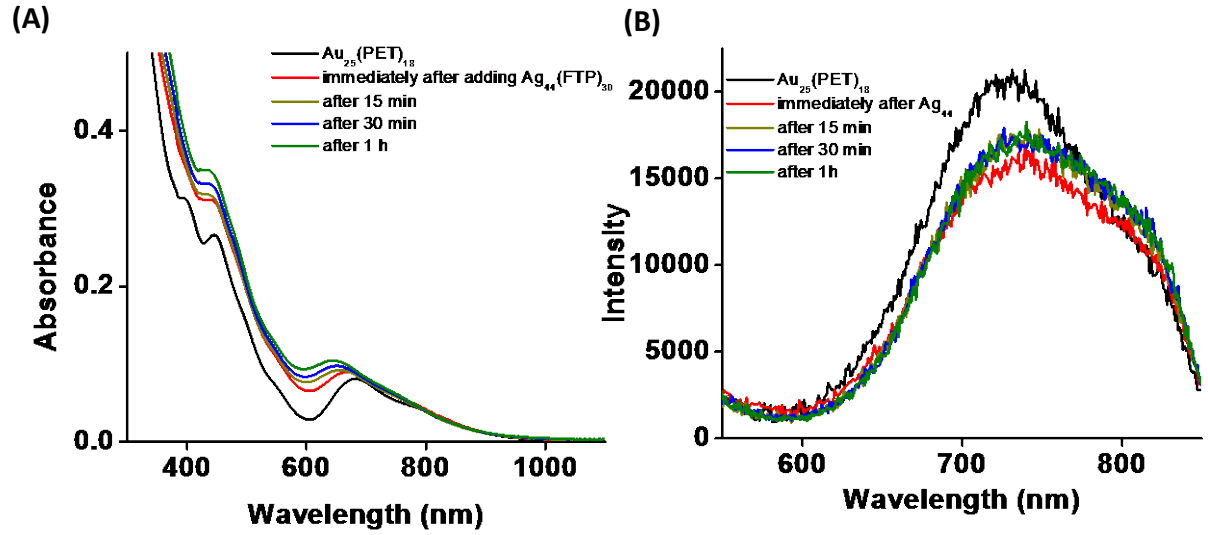

Figure S12. Time-dependent changes in the UV/Vis (A) and emission (B) spectra during the reaction between $Au_{25}(PET)_{18}$ and $Ag_{44}(FTP)_{30}$ clusters taken in the ratio (Au_{25}:Ag_{44}) of 14:1. Solvent used was dichloromethane.

Note: Emission spectrum of $Au_{25}(PET)_{18}^{-}$ shows a peak at 720 nm and a hump at 800 nm as reported previously by Jin et al.[9] When $Ag_{44}(FTP)_{30}$ was added to $Au_{25}(PET)_{18}$, in all the cases (Figures S12-S14), there was an immediate decrease in intensity of these features. But, as time goes on, intensity increased with a slight redshift of about 10 nm (for both features).

Supporting Information 10

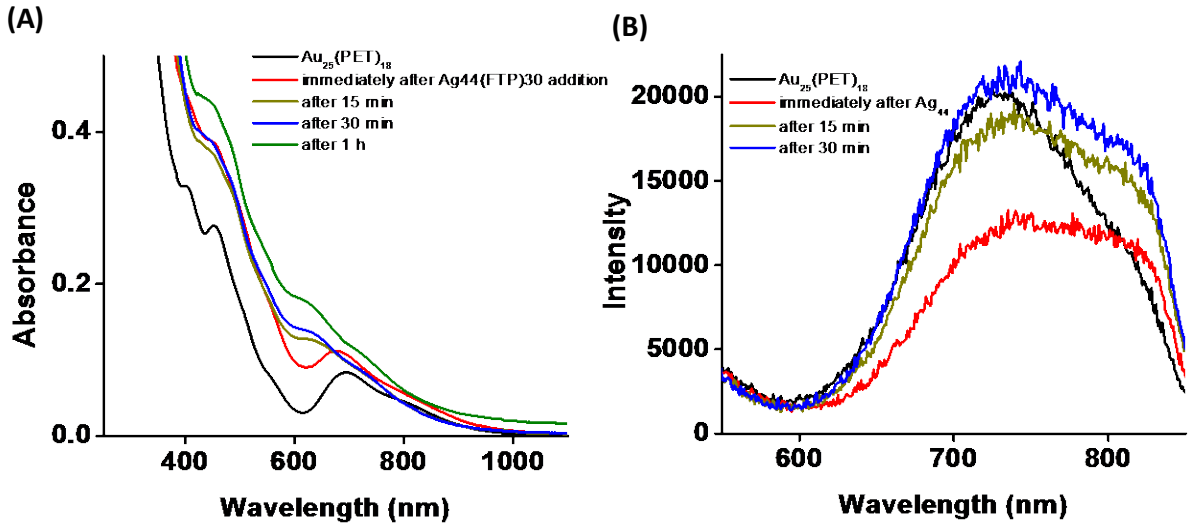

Figure S13. Time-dependent UV/Vis spectra (A) and emission (B) spectra during the reaction between $Au_{25}(PET)_{18}$ and $Ag_{44}(FTP)_{30}$ clusters taken in the ratio (Au_{25}:Ag_{44}) of 7:1.

Supporting Information 11

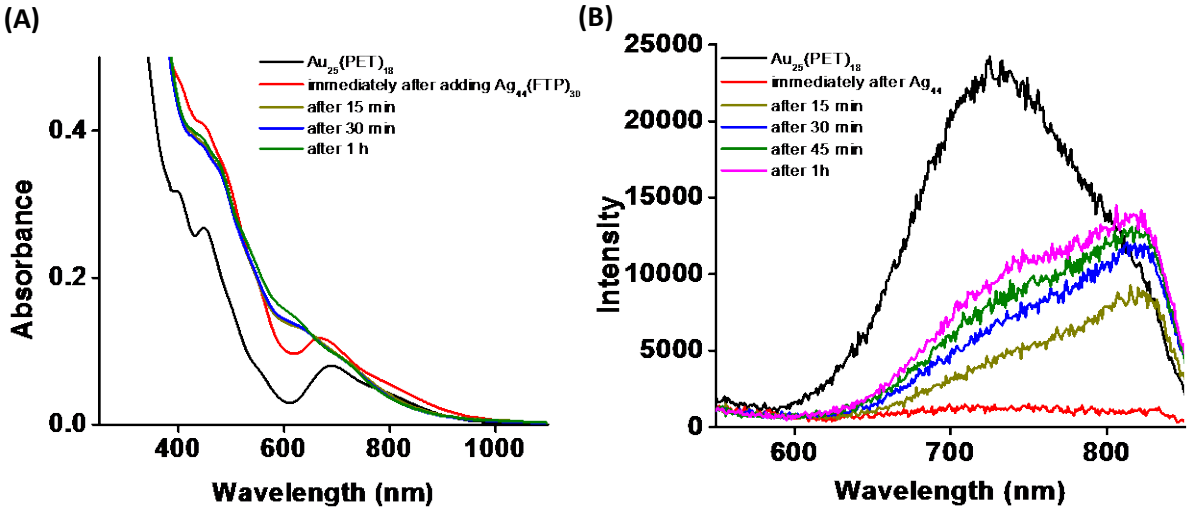

Figure S14. Time-dependent UV/Vis spectra (A) and emission (B) spectra during the reaction between $Au_{25}(PET)_{18}$ and $Ag_{44}(FTP)_{30}$ clusters taken in the ratio (Au_{25}:Ag_{44}) of 1.7:1.0.

Supporting Information 12

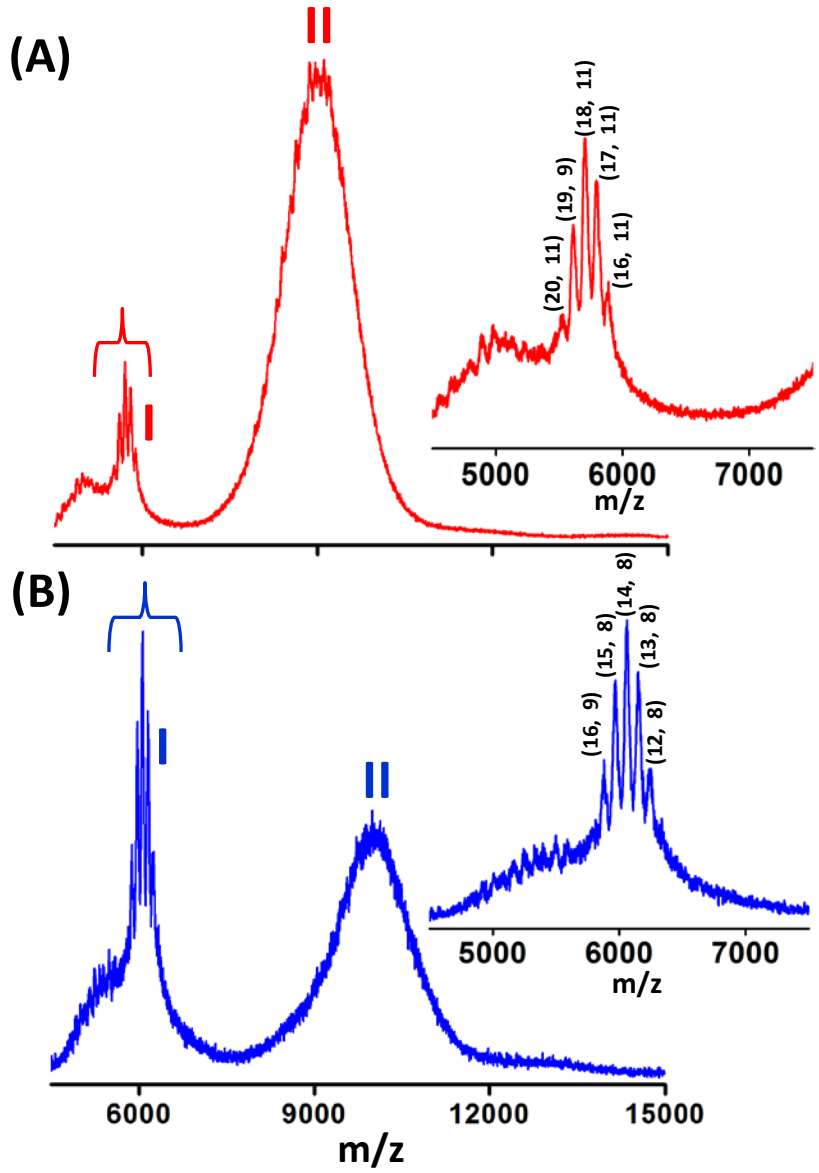

Figure S15. Negative ion mode MALDI MS spectra of the $Au_{25-x}Ag_x(PET)_{18-y}(FTP)_y$ (x=0,1-13; y=0,1-8) product clusters formed at $Au_{25}(PET)_{18}$:$Ag_{44}(FTP)_{30}$ ratio of (A) 0.7:1 and (B)1:1. Group I is expanded in the inset. The numbers (x, y) in parenthesis (in the insets), are according to the general molecular formula, $Au_{25-x}Ag_x(PET)_{18-y}(FTP)_y$.

Supporting Information 13

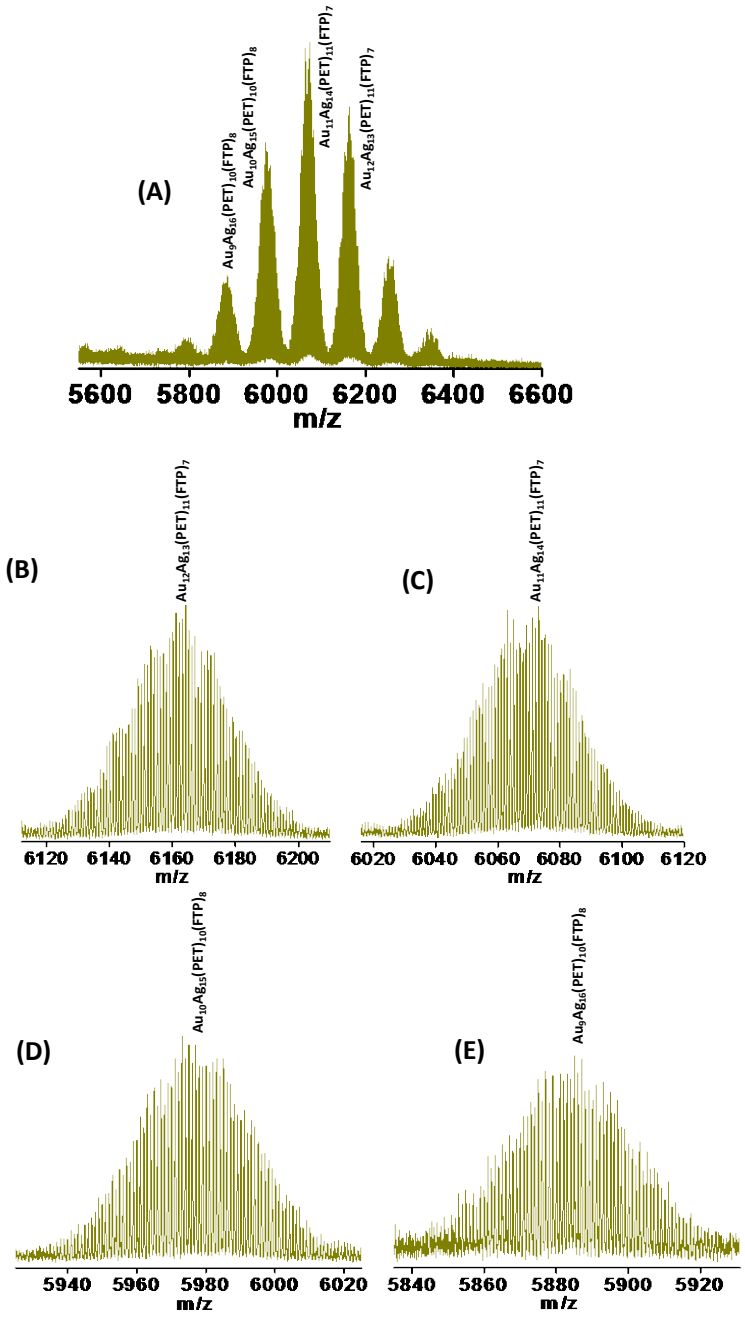

Figure S16. ESI MS spectrum of the mixture of $Au_{25}(PET)_{18}$ and $Ag_{44}(FTP)_{30}$ (in Au_{25}:Ag_{44} ratio 1:1) measured 1h after mixing. Features labelled in panel A are expanded in panels B-E. The peak labels in B-E are given according to the peak maxima in each bunch. However, due to large number of Ag atoms and resulting isotopic width, features within these bunches are not resolved fully (unlike in the Figure S6 and S7).

Supporting Information 14

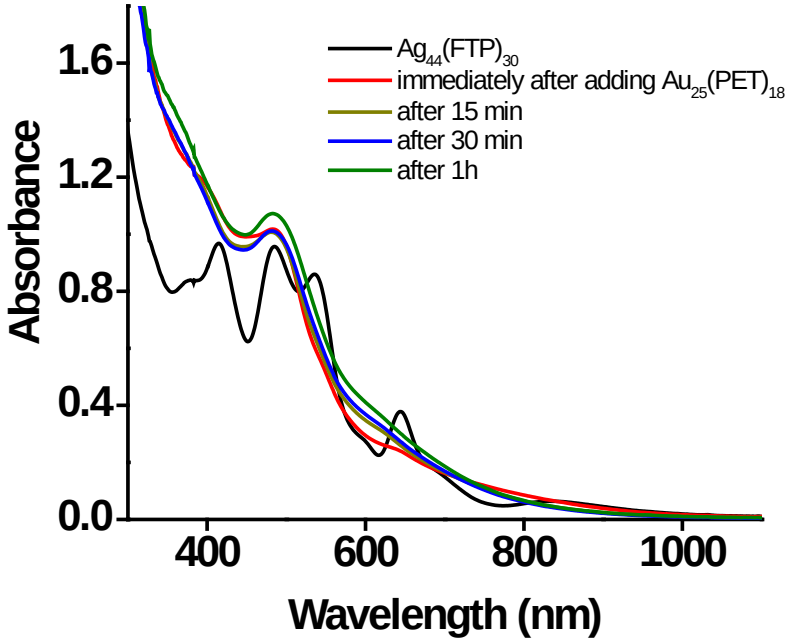

Figure S17. Time-dependent UV/Vis spectra during the reaction between $Au_{25}(PET)_{18}$ and $Ag_{44}(FTP)_{30}$ clusters taken in the ratio (Au_{25}:Ag_{44}) of 1.0:1.0.

Supporting Information 15

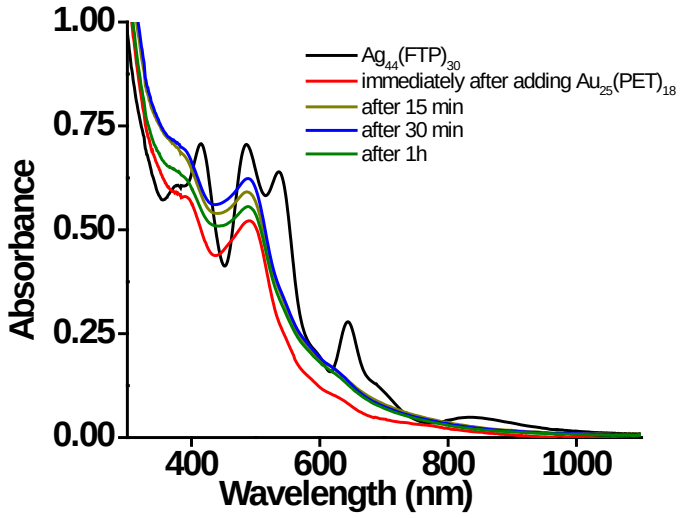

Figure S18. Time-dependent UV/Vis spectra during the reaction between $Au_{25}(PET)_{18}$ and $Ag_{44}(FTP)_{30}$ clusters taken in the ratio (Au_{25}:Ag_{44}) of 0.7:1.0.

Supporting Information 16

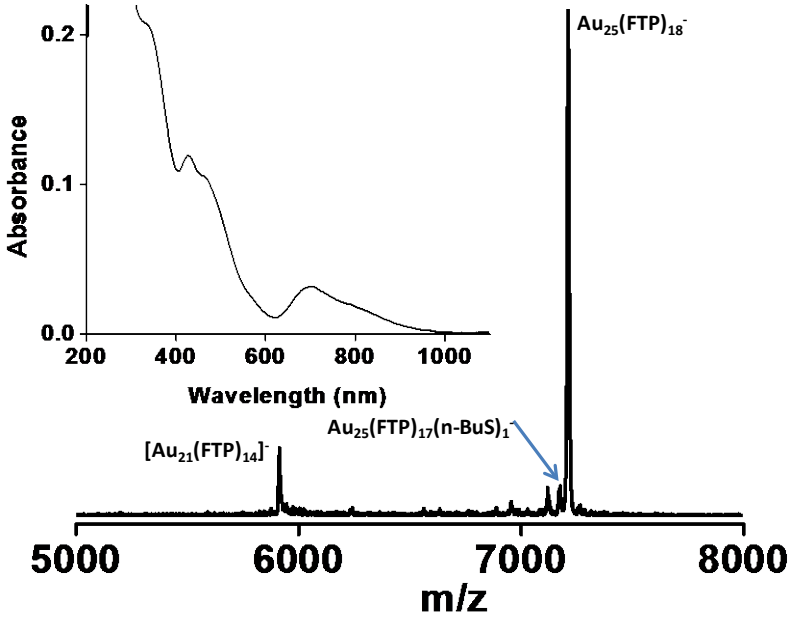

Figure S19. MALDI MS of the $Au_{25}(FTP)_{18}$ clusters synthesized through ligand exchange of $Au_{25}(n\text{-}BuS)_{18}$ with 4-fluorothiophenol. Inset shows the UV/Vis spectrum of $Au_{25}(FTP)_{18}$.

Supporting Information 17

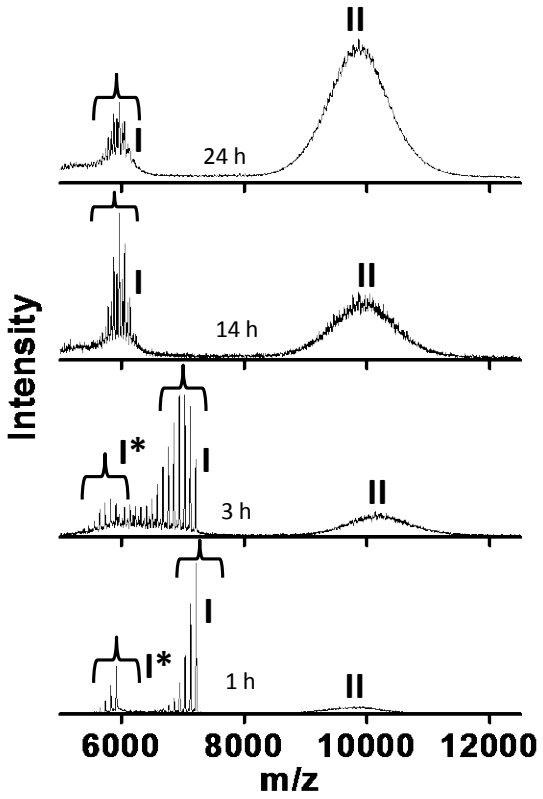

Figure S20. Time-dependent changes in the MALDI MS spectra of the products formed during the reaction between $Au_{25}(FTP)_{18}$ and$Ag_{44}(FTP)_{30}$. The spectra for 1 h and 3 h are shown in the main manuscript (Figure 4). The spectrum for 24 h is shown in the Figure S21.

Note: Comparison of group I in Figures S3-S5 and S20 reveal that there is a drastic difference in rates of reactions between Au and Ag clusters depending on whether the same or different ligand is used to protect them. Time-dependent MALDI MS measurements show that irrespective of the concentrations of the reactant clusters, the reaction between $Au_{25}(PET)_{18}$ and $Ag_{44}(FTP)_{30}$ got completed/equilibrated within 10-15 min. In contrast, the reaction between $Au_{25}(FTP)_{18}$ and $Ag_{44}(FTP)_{30}$ continued for several hours (Figure S20). During the reaction between clusters with different ligands, the mass spectra show peaks arising from the inclusion of one to several Ag atoms, which in turn transform to only 3-4 prominent peaks after about ten minutes. But in the case of clusters having thesame ligands, only 1-6 Ag inclusions are observed in group I even after 1 h of the reaction. When the ligands are different, the inter-cluster reaction may be initiated by a fast (Au-SR)–(Ag-SR′) exchange step, starting the disruption of the thiolate staples. This in turn can make the clusters unstable leading to the incorporation of Ag and ligands. Thus, we believe that the nature of the ligand shell on the reactant clusters play an important role in controlling the reactivity of the clusters.

Supporting Information 18

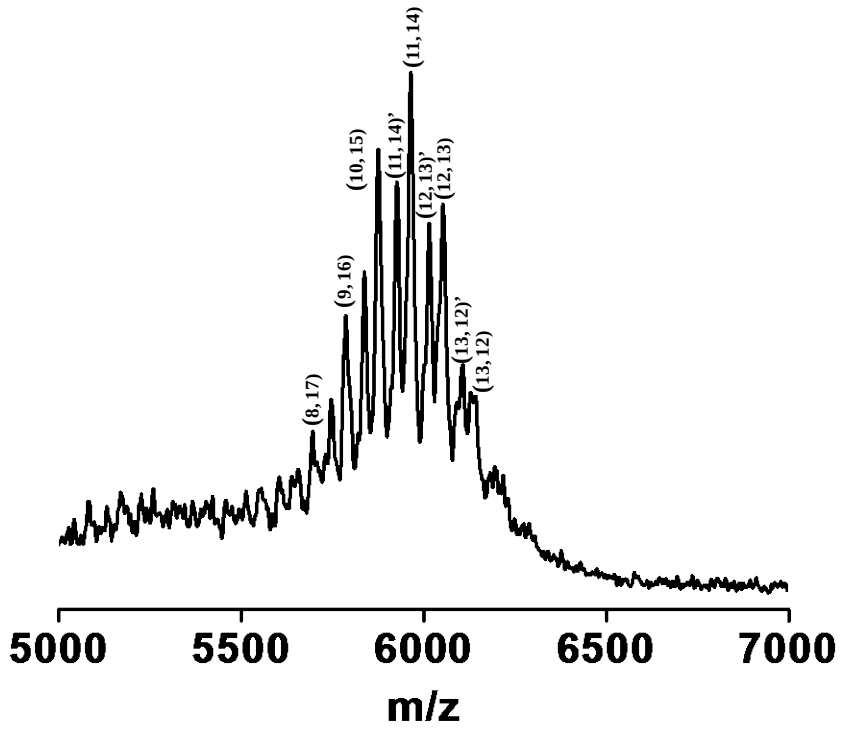

Figure S21. MALDI MS spectra of the clusters formed after 24 h (expansion of the group I in the uppermost panel, i.e., spectrum for 24 h, Figure S20) the reaction between $Au_{25}(FTP)_{18}$ and $Ag_{44}(FTP)_{30}$. The peaks labeled as (13, 12)', (12, 13)', etc., are due to the exchange of a single FTP ligand in (13, 12) and (12, 13) clusters with a single n-BuS ligand (mass difference between these peaks are 38 Da, M_{FTP}-$M_{n\text{-}BuS}$). The numbers in parenthesis, (m, n), are according to the general molecular formula, $Au_mAg_n(FTP)_{18}$.

Supporting Information 19

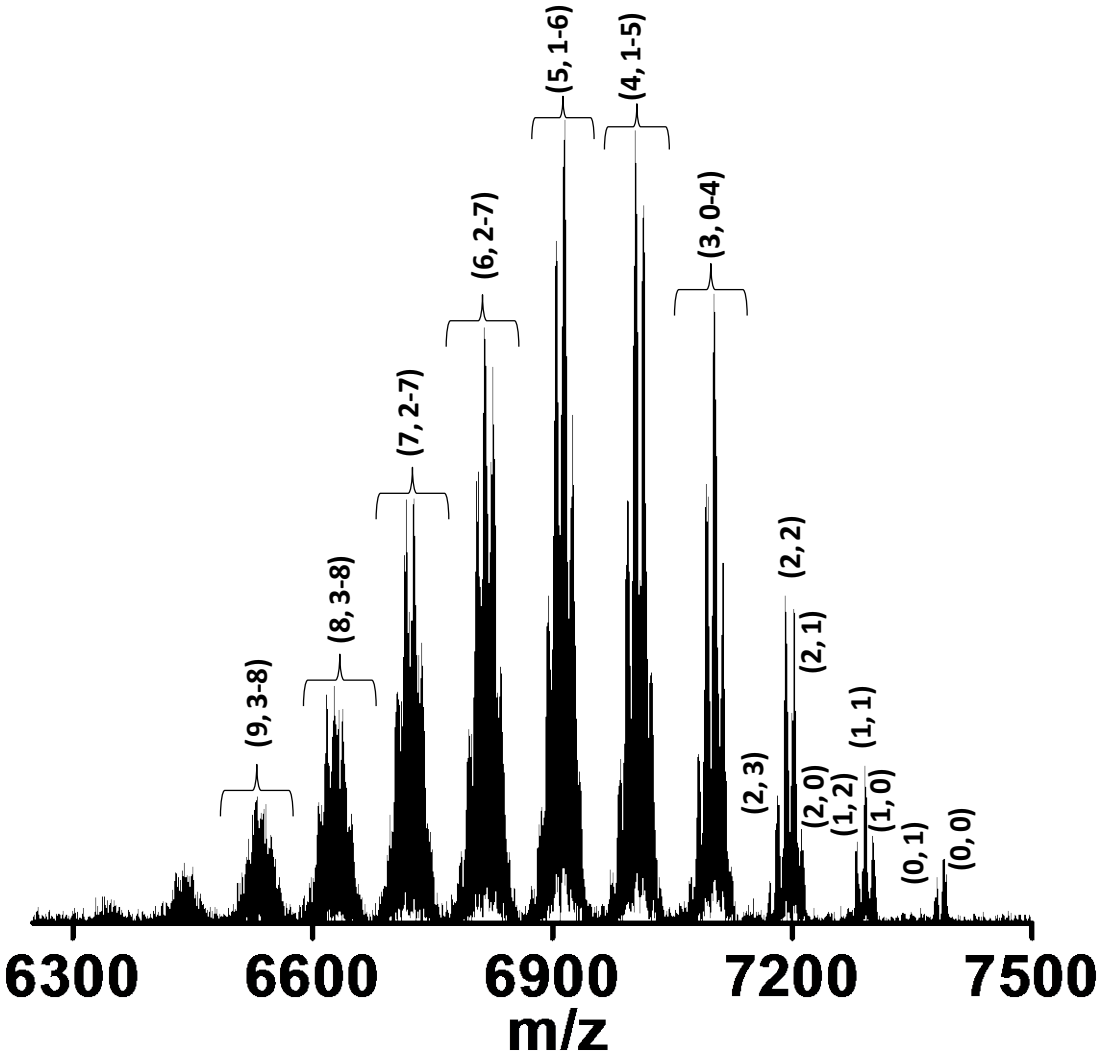

Figure S22: ESI MS spectra measured immediately after mixing $Au_{25}(PET)_{18}$ and $Ag_{44}(FTP)_{30}$ at a Au_{25}:Ag_{44} ratio of 1.7:1. The numbers (x, y) in parenthesis are according to the general molecular formula, $Au_{25-x}Ag_x(PET)_{18-y}(FTP)_y$.

Supporting Information 20

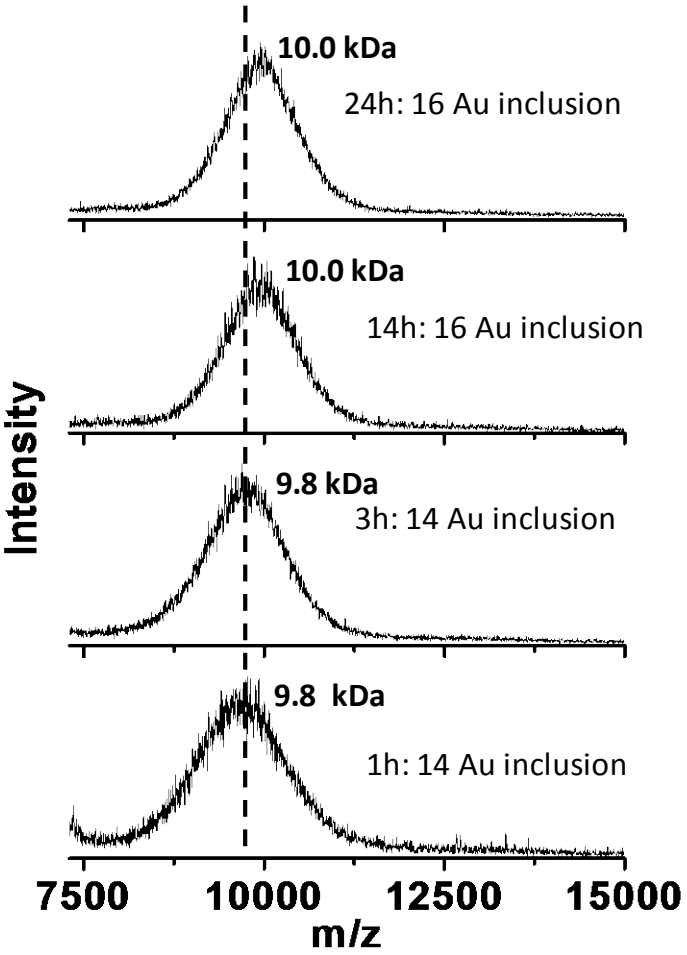

Figure S23. Time-dependent changes of group II features appeared in the MALDI MS spectra during the reaction of $Ag_{44}(FTP)_{30}$ and $Au_{25}(PET)_{18}$. Groups II in Figure S20 are expanded here. A gradual shift of the peak maxima to higher m/z is seen.

Supporting Information 21

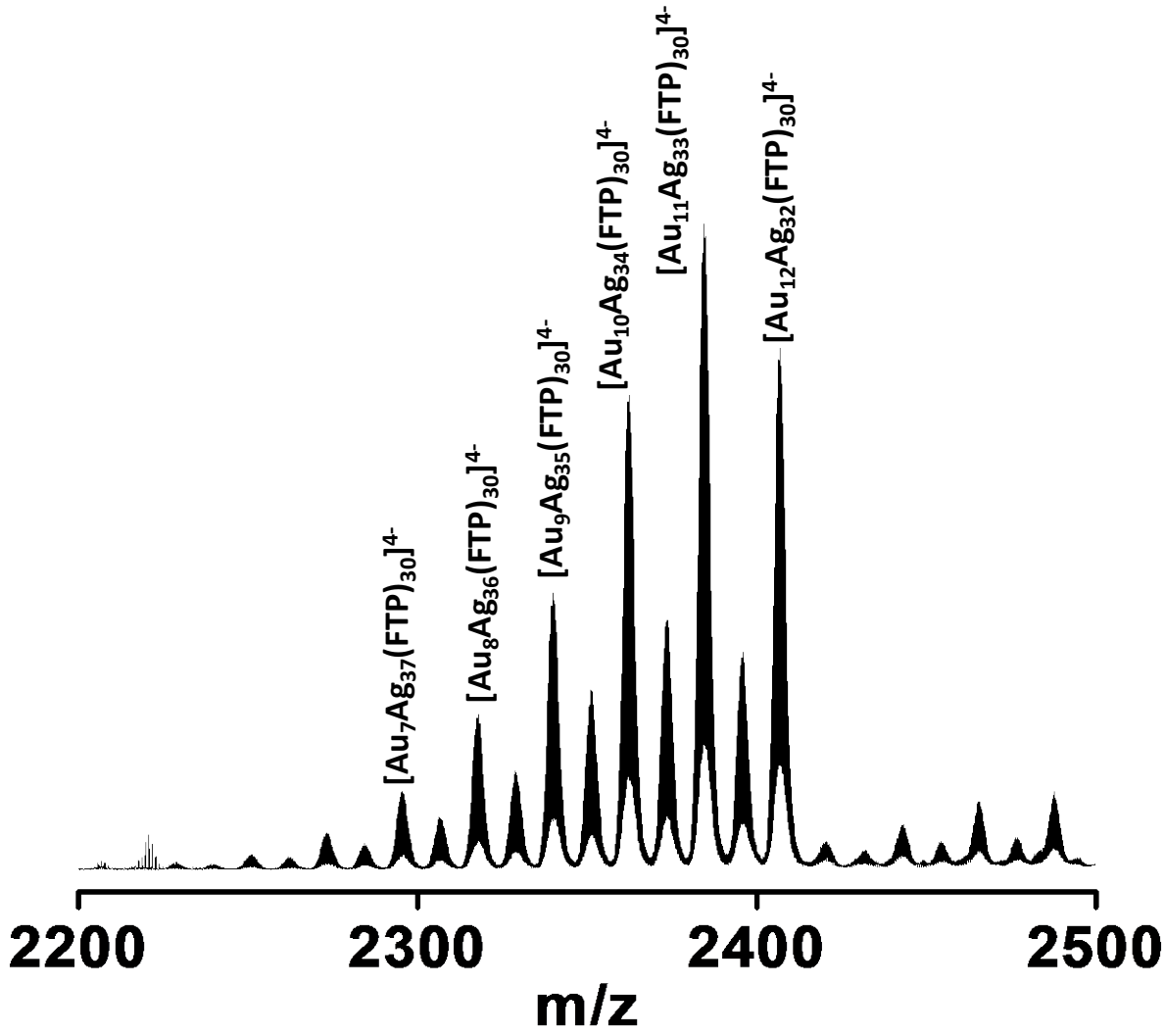

Figure S24. ESI MS spectra showing the formation of $Au_xAg_{44-x}(FTP)_{30}$ during the reaction between $Au_{25}(FTP)_{18}$ and $Ag_{44}(FTP)_{30}$ at a Au_{25}:Ag_{44} ratio of 0.7:1.0. The peaks in between are due to the n-butanethiol-containing Au_xAg_{44-x} species as the latter could not be completely removed from $Au_{25}(FTP)_{18}$ (see Figure S21).

Supporting Information 22

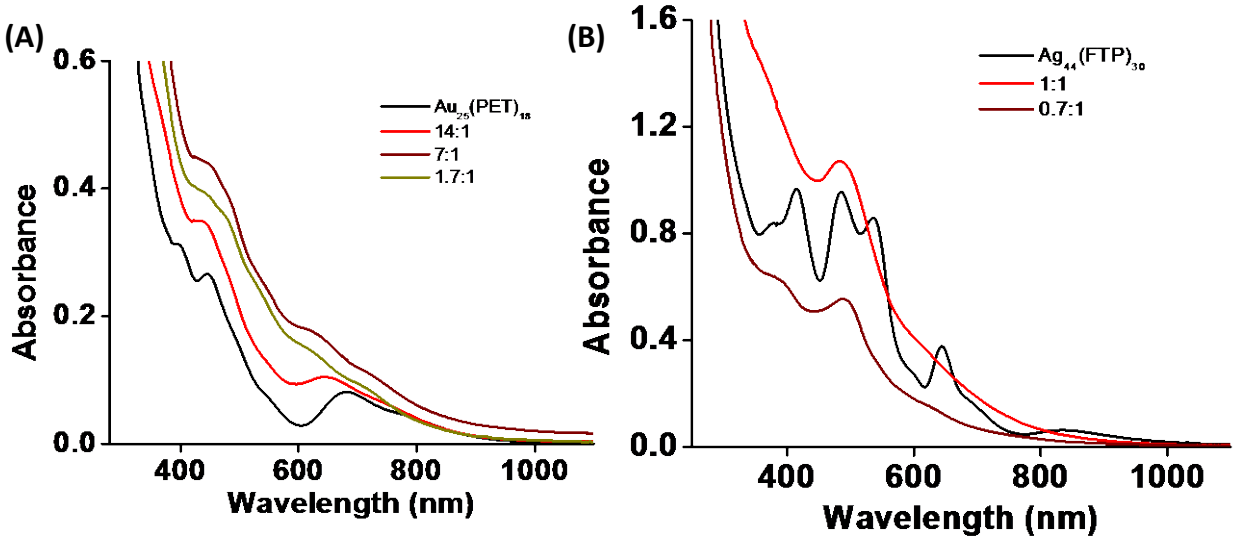

Figure S25. UV/Vis spectra of the reaction mixtures (after 1h of the reaction) at Au_{25}:Ag_{44} ratios of 14:1, 7:1, 1.7:1 (A) and 1:1 and 0.7:1 (B). At lower Ag_{44} concentrations (in A) the spectra resembles more with the previously reported spectra of $Au_{25-x}Ag_x(SR)_{18}$ (see Ref. 16 in main manuscript). At higher concentrations of Ag_{44} (in B), the spectra resembles more with the previously reported spectra of $Au_xAg_{44-x}(SR)_{30}$ (see Ref. 15 in the Article).

Supporting Information 23

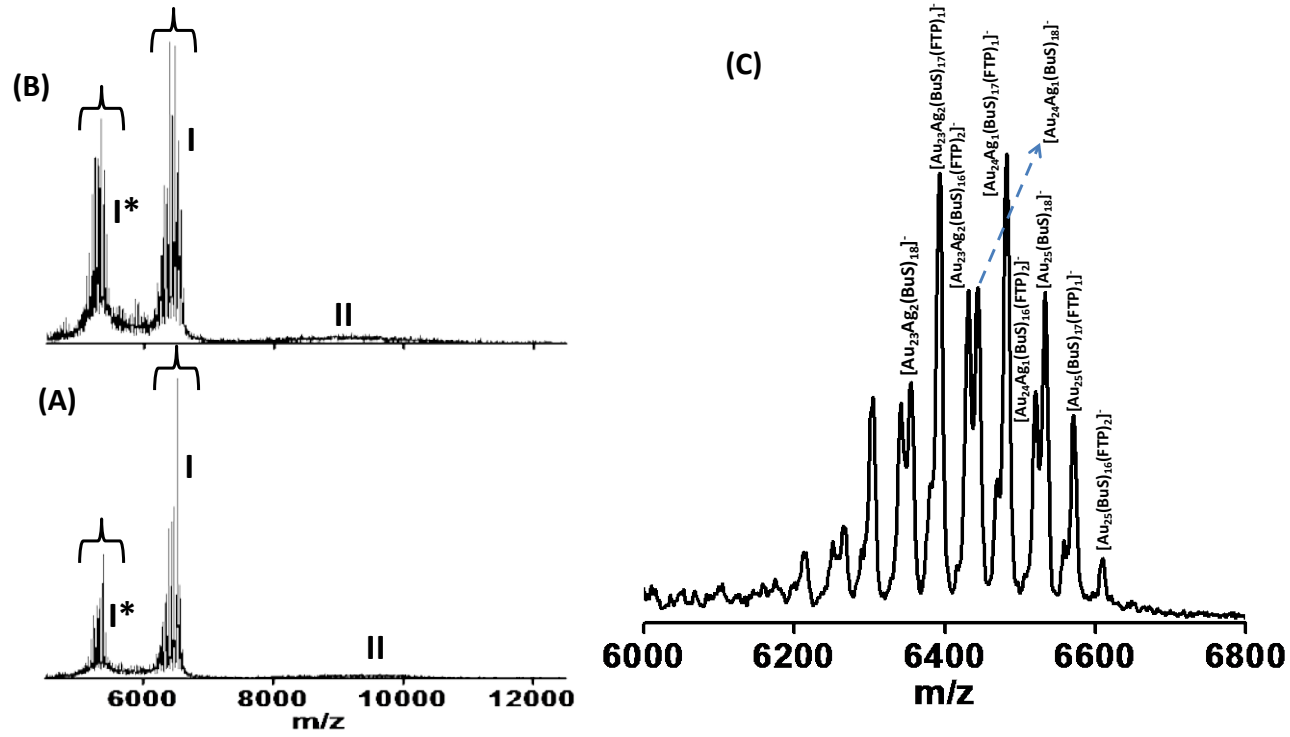

Figure S26. Negative ion mode MALDI MS spectra of the products formed immediately (A) and after 1h (B) of mixing Au_{25}(n-BuS)$_{18}$ and Ag_{44}(FTP)$_{30}$ clusters in dichloromethane. Group I in B is expanded in C. Group I are the molecular ion peak of the alloy clusters with mixed ligands formed during the reaction and the group I* are due to their fragments (due to $Au_4(SR)_4$ loss). Peaks due to BuS-FTP, Ag-Au and (Ag-FTP)-(Au-BuS) exchanges are labeled in C.

Supporting Information 24

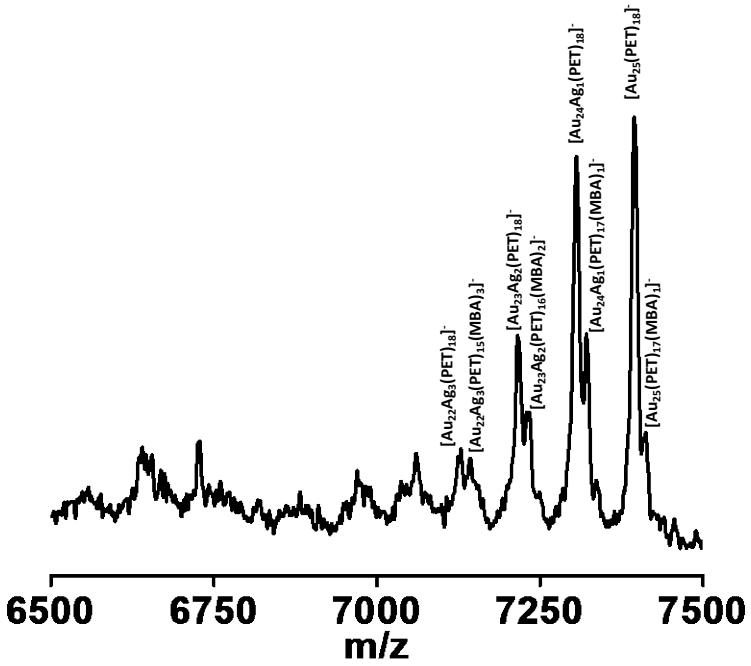

Figure S27. MALDI MS spectra of the products formed immediately after mixing $Au_{25}(PET)_{18}$ and $Ag_{44}(MBA)_{30}$ clusters. Peaks due to MBA-PET, Ag-Au and (Ag-MBA)-(Au-PET) exchanges are marked.

Supporting Information 25

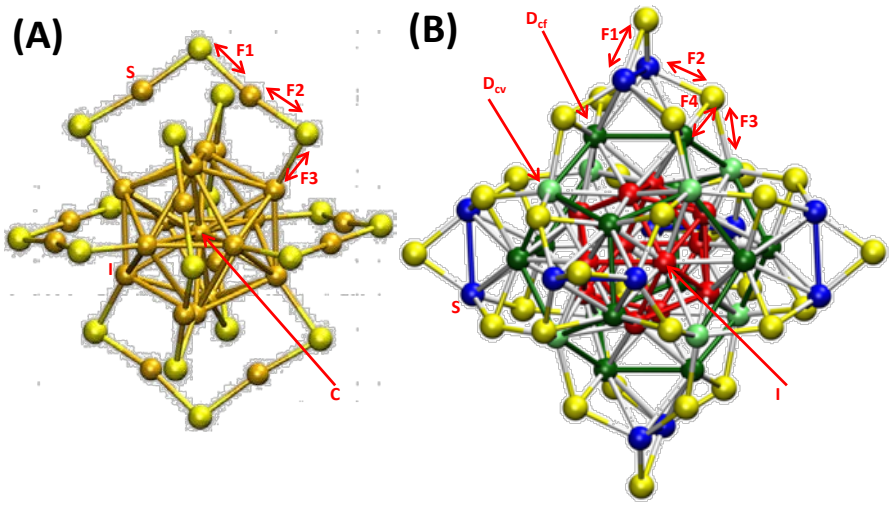

Figure S28. Structures of (A) $Au_{25}(SR)_{18}$ and (B) $Ag_{44}(SR)_{30}$ showing different types of Ag/Au atoms and Ag-S/Au-S bonds. Color codes of Ag atoms: staple (blue), dodecahedron (light and dark green), icosahedron (red). Au atoms are in orange and S atoms are in light yellow. Light green Ag atoms forms the vertices of the cube of the Au_{20} dodecahedron and the darker green

Ag atoms are at the faces of this cube. The labels F1-F4 correspond to different types of Ag-S/Au-S bonds. In $Ag_{44}(SR)_{30}$, F1 involves the terminal ligand while the others involve the bridging ligand. In F3 the bridging ligand binds to the Ag atoms in the cube vertices of the dodecahedron (D_{cv}). In F4 the bridging ligand binds to the cube faces of dodecahedron (D_{cf}).

Supporting Information 26: Results of theoretical calculations

Table S1: Isomers of $Ag_{43}Au(SH)_{30}$ and their energies

Isomer	**Au location**	**Energy E/eV**	**E-E_0/eV**
I	Central icosahedron	-349.995	-0.72
D_{cv}	Dodecahedron (cube vertex)	-349.416	-0.14
D_{cf}	Dodecahedron(cube face)	-349.592	-0.32
S	Staple	-349.754	-0.48

Table S2: Isomers of $Au_{24}Ag(SH)_{18}$ and their energies

Isomer	**Ag location**	**Energy E/eV**	**E-E_0/eV**
C	Centre of icosahedron	-219.576	+0.71
I	Icosahedron	-220.047	+0.23
S	Staple	-219.837	+0.44

Table S3: Energies of undoped clusters, metal atoms, and metal-ligand fragments

Structure	**E_0/eV**
$Ag_{44}(SH)_{30}$	-349.275
$Au_{25}(SH)_{18}$	-220.281
Ag	-0.1862
Au	-0.2035
AgSH	-8.658
AuSH	-8.902

Table S4. Energies of the reaction, $Au + Ag_{44}(SR)_{30} \rightarrow AuAg_{43}(SR)_{30} + Ag$

Isomer	Position of Au in $AuAg_{43}(SR)_{30}$	Energy E/eV
I	Inner icosahedron	-0.70
D_{cv}	Dodecahedron Cube vertex	-0.12
D_{cf}	Dodecahedron Cube face	-0.30
S	Staples	-0.46

Table S5. Energies of the reaction, $Au\text{-}SR + Ag_{44}(SR)_{30} \rightarrow AuAg_{43}(SR)_{30} + Ag\text{-}SR$

Position of Au-SR in $AuAg_{43}(SR)_{30}$	Energy E/eV
Dodecahedron Cube vertex (F3)	+0.10
Dodecahedron Cube face (F4)	-0.07
Staples (F1 and F2)	-0.24

Table S6. Energies of the reaction, $Ag + Au_{25}(SR)_{18} \rightarrow Au_{24}Ag(SR)_{18} + Au$

Isomer	Position of Ag in $Au_{24}Ag(SR)_{18}$	EnergyE/eV
C	Centre of icosahedron	+0.69
I	Icosahedron	+0.22
S	Staples	+0.43

Table S7. Energies of reaction, $Ag\text{-}SR + Au_{25}(SR)_{18} \rightarrow Au_{24}Ag(SR)_{18} + Au\text{-}SR$

Position of Ag-SR in $Au_{24}Ag(SR)_{18}$	EnergyE/eV
Icosahedron (F3)	-0.01
Staples (F1 and F2)	+0.2

Table S8. HOMO-LUMO energy difference of un-exchanged and alloy clusters

Cluster	Metal substituent position	HOMO/eV	LUMO/eV	HOMO-LUMO Gap/eV	Fermi Energy/eV
$Ag_{44}(SH)_{30}$	none	2.59	3.45	0.86	3.01
$Ag_{43}Au(SH)_{30}$	I	2.57	3.44	0.87	3.01
$Ag_{43}Au(SH)_{30}$	D_{cv}	2.61	3.43	0.82	3.02
$Ag_{43}Au(SH)_{30}$	D_{cf}	2.63	3.44	0.81	3.04
$Ag_{43}Au(SH)_{30}$	S	2.63	3.44	0.81	3.04
$Au_{25}(SH)_{18}$	none	-2.53	-1.24	1.29	-1.88
$Au_{24}Ag(SH)_{18}$	C	-2.49	-1.35	1.14	-1.92
$Au_{24}Ag(SH)_{18}$	I	-2.51	-1.22	1.28	-1.86
$Au_{24}Ag(SH)_{18}$	S	-2.56	-1.30	1.26	-1.93

Table S9. Energy difference (in eV) between the HOMO of $AuAg_{43}(SR)_{30}$ and LUMO of $Au_{24}Ag\ (SR)_{18}$ as a function of the substituent positions. The values showed in bold are those for the most favorable combinations of substituent positions.

Au Position in Ag_{44} / **Ag Position in Au_{25}**	**I**	**D_{cv}**	**D_{cf}**	**S**
C	3.92	3.96	3.98	3.98
I	**3.79**	3.83	3.86	**3.85**
S	**3.87**	3.91	3.93	3.93

Supporting Information 27

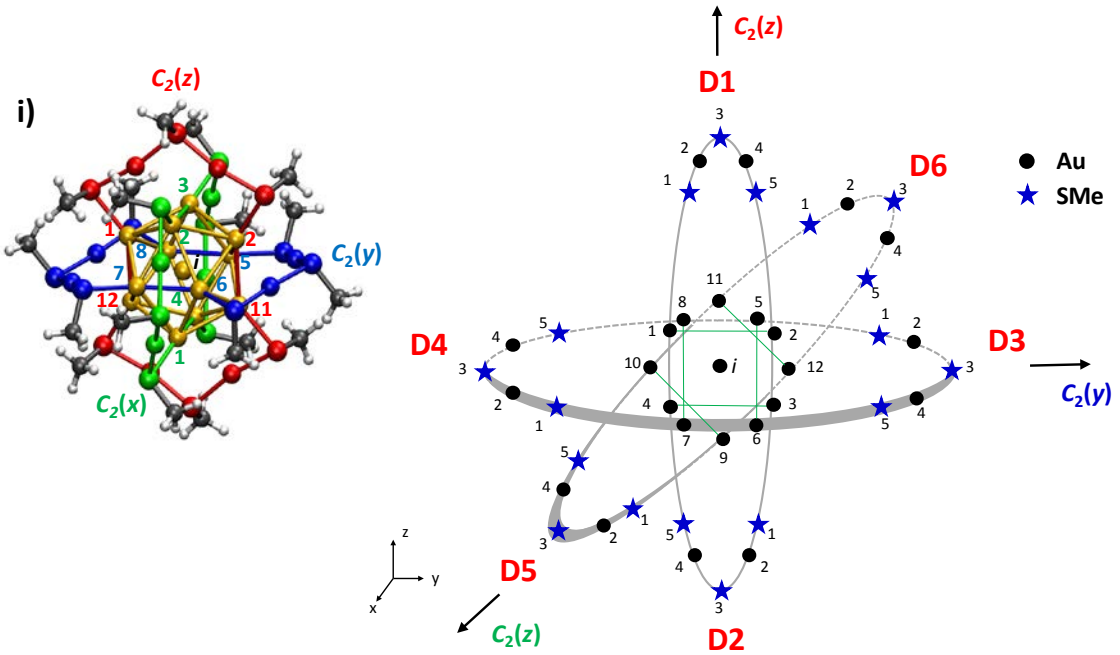

Figure S29. Borromean-Rings diagram of $Au_{25}(SMe)_{18}$. The rings formed by pairs of coplanar staples are shown as ellipses. Gold atoms are shown by black dots and dark blue stars represent the SMe ligands whose positions are taken to be identical with their sulfur atom.The core Au atoms are numbered from 1 to 12 and the staple atoms are numbered clockwise from end of the staple, from 1 to 5. The lines that join core Au atoms on opposite ends of the same staple are shown by the green lines. The three perpendicular C_2 axes are marked with the associated Cartesian axis direction in brackets. The staple directions are labeled by the six staple locants D1 to D6, marked in red. Inset (i) shows a 3D visualization of the ring structure of the core and staples of $Au_{25}(SR)_{18}$ aspicule, with each (Au_8S_6)-ring consisting of two coplanar staples and the core atoms that are bonded to these staples. The three rings are colored red, blue and green, and the numbers of the core atoms are marked. This figure and caption are adapted from Ref. 20 of the main manuscript.

Supporting Information 28

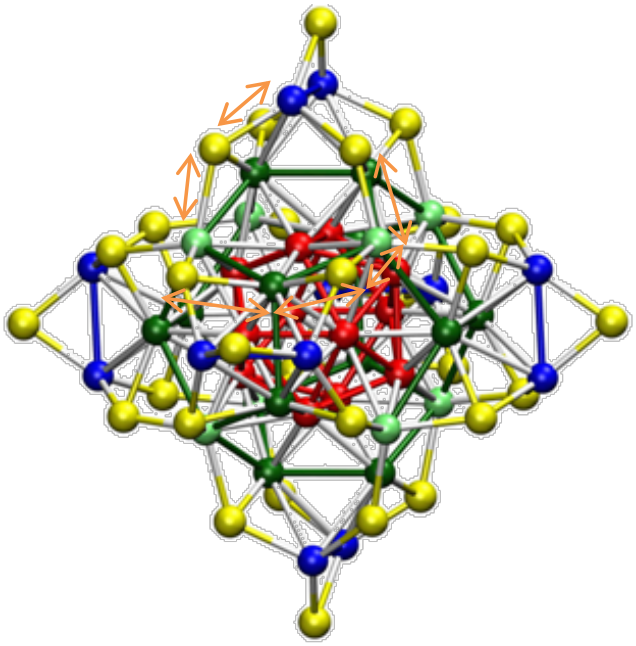

Figure S30. Structure of $Ag_{44}(SR)_{30}$ showing the accessibility of the icosahedral core Ag atoms. The bonds marked with orange arrows when broken make the core atoms more exposed.

Supporting Information 29

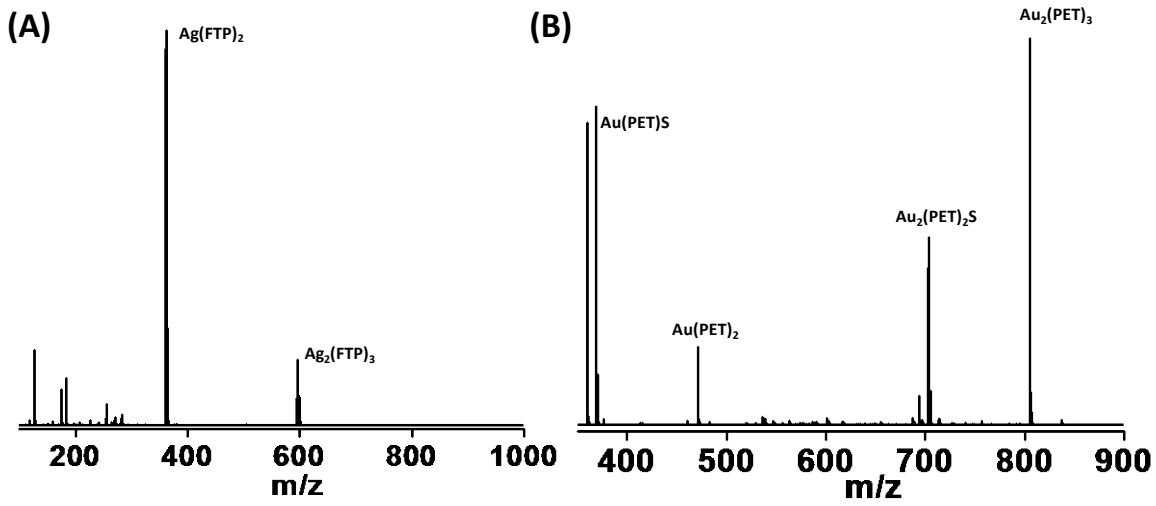

Figure S31. Mass spectra showing the thiolate fragments of (A) $Ag_{44}(FTP)_{30}$ and (B) $Au_{25}(PET)_{18}$.

Supporting Information 30: Schematic of the reaction between $Au_{25}(SR_1)_2$ with $Ag(SR_2)_2$

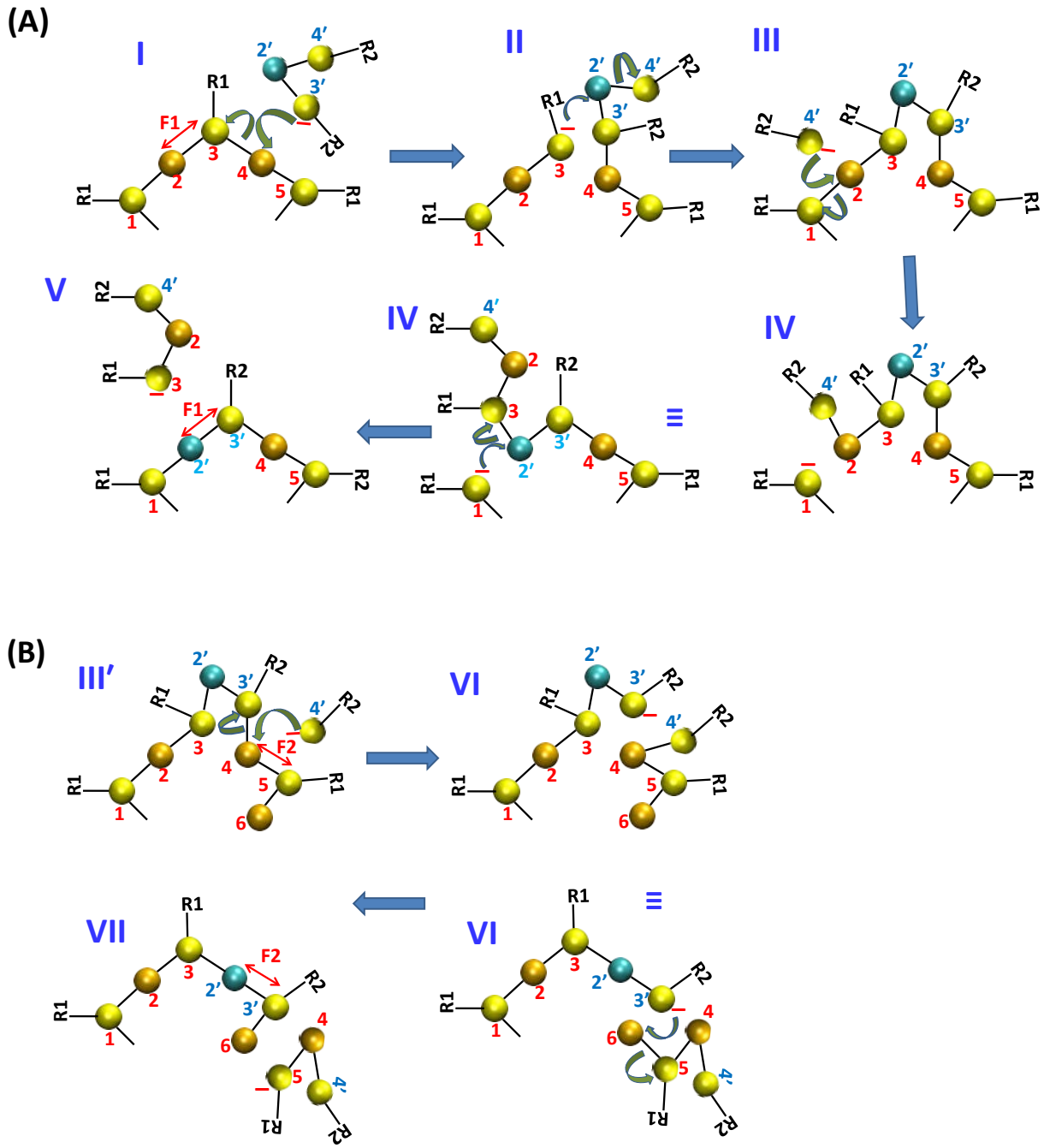

Scheme S1. Schematic of the reaction between $Ag(SR_2)_2$ anion and the staples of $Au_{25}(SR_1)_{18}$ resulting in exchange of (A) fragment F1 (B) fragment F2. Color codes of the atoms: dark yellow (Au), light yellow (S), blue (Ag). Au and sulfur atoms in the staple are numbered from 1 to 5 (red). Gold atom labeled as 6 is part of the icosahedral core. Atoms in the $Ag(SR_2)_2$ are labeled as 2′, 3′ and 4′ (blue). Structures in the intermediate steps are labeled I to VII. Comparison of structures I and V in (A) shows that the fragment F1 was exchanged between the staples and

fragment. Comparison of structures III′ and VII shows that the fragment F2 was exchanged between the staple and fragment.

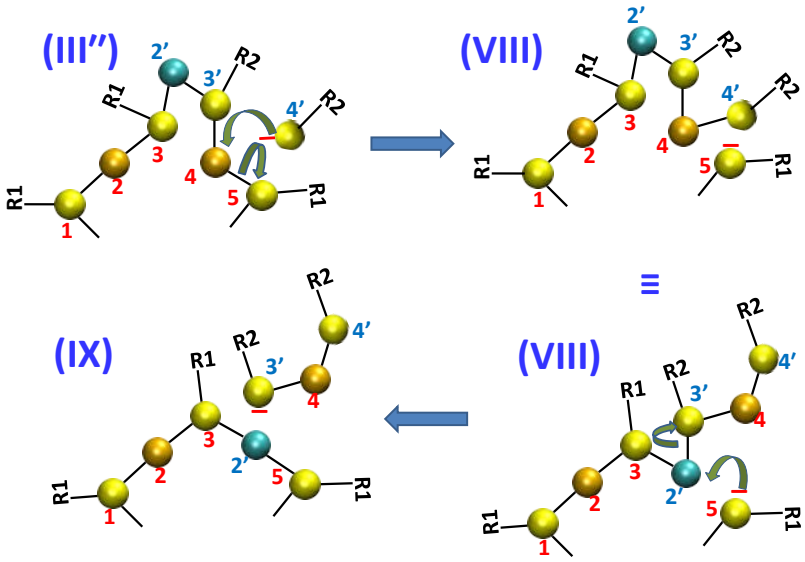

Scheme S2. Schematic of the reaction between $Ag(SR_2)_2$ anion and the staples of $Au_{25}(SR_1)_{18}$ resulting in Ag/Au exchange. Color codes of the atoms: dark yellow (Au), light yellow (S), blue (Ag). Au and sulfur atoms in the staple are numbered from 1 to 5 (red). Atoms in the $Ag(SR_2)_2$ are labeled as 2′, 3′ and 4′ (blue). Comparison of the structures III″ and IX show that Au atom (4) is exchanged with Ag atom (2′).

Note: Structures III, III′ and III″ differ only in the position of attack of the R_2S^- and the subequent bond breaking steps. Also note that structures having the same labels labels (IV, VIII) are identical and differ only in their orientation. Similar to the schemes S1 and S2, it is possible to draw mechanistic pathways showing the replacement of Au atoms in the icosahedral core (atoms labeled 6, for example) also. But there will be significant steric effects in the various steps.

Discussion on the charge states of $Au_{25}(SR)_{18}$ and the position of Ag in the $Au_{25-x}Ag_x(PET)_{18-y}(FTP)_y$:

$Au_{25}(SR)_{18}$ exists in two most stable charge states: neutral and anionic.[10] Crystal structures of both the anionic and neutral $Au_{25}(SR)_{18}$ have been solved.[4,10a] In the anion,12 of the 25Au atoms are part of six $Au_2(SR)_3$ staples and they are in +1 oxidation state. The 12 terminal sulfurs of the six $Au_2(SR)_3$ staples bind to the 12 icosahedral core Au (Au_{core}) atoms. Among these twelve S_{staple}-Au_{core} bonds, six of them localize the valence electrons of those six Au_{core} atoms. The remaining six valence electrons of the Au_{13} core, in addition to that of the central Au and the negative charge, provide eight free electrons fulfilling the magic number criterion for electronic stability. Thus, only seven of the icosahedral Au atoms contribute to the free electron count of the anionic Au_{25}. This implies that any substitution of the Au_{staple} with another metal like Ag (having a similar electronic configuration) will not reduce the free electron count and the overall charge of the bimetallic cluster because Ag is likely to exist as Ag(I) in the staples rather than as Ag(0), similar to the Au(I) in $Au_2(SR)_3$ staples. Substitution of Au_{core} with Ag can alter the free electron count depending upon the nature of Au (i.e., whether the Au is strongly or weakly bound to S_{staple}) that is being replaced and the oxidation state of the incoming Ag (whether Ag(I) or neutral Ag). $Ag_xAu_{25-x}(SR)_{18}$ (x<6) clusters synthesized by co-reduction of $HAuCl_4$ and $AgNO_3$ by sodium borohydride are also anionic with eight free electrons as in case of undoped anionic $Au_{25}(SR)_{18}$. Experimental observations and theoretical calculations[11] on these clusters show that the incoming Ag atoms are preferably located at the icosahedral positions, replacing the Au_{core} atoms. These observations show that the incoming Ag (upto 6) atoms are present in the icosahedral positions of $Ag_xAu_{25-x}(SR)_{18}$ as Ag(0), not as Ag(I). This reduction of the Ag(I) to Ag(0) could be due to the external reducing agent used.

As opposed to the above case, reaction of anionic $Au_{25}(PET)_{18}$ with Ag(I) salts in acetonitrile results in the formation of neutral $Au_{25}Ag_2(PET)_{18}$ and its structure has been predicted through DFT calculations.[12]These calculations show that one of the two incoming Ag(I) is incorporated into the thiolate shell of the clusters as Ag(I)-SR which does not alter the free electron count. The second Ag(I) is situated outside the Au_{13} core and it is bonded to one of the Au_{core} atoms. The bonding of this Ag(I) to icosahedral Au_{core} decreases the free electron count by one. Hence, anionic $Au_{25}(PET)_{18}$ produces neutral $Au_{25}Ag_2(PET)_{18}$ clusters due to its reaction with Ag(I). Thus, it is obvious that incorporation of metals, with similar electronic configuration as Au, into $Au_{25}(SR)_{18}$ using their cationic precursors in the absence of an external reducing agent will reduce the free electron count if the dopant metal makes any electron localizing bonds to Au_{core}. Further, the report of $Au_{25}Ag_2(SR)_{18}$ suggests that the positions of the dopant atoms/ionsin the bimetallic clusters vary depending on the nature of the precursors and reaction conditions (whether any external reducing agent is used or not).

In this regard, it is worthwhile to understand the nature of the incoming Ag in the inter-cluster reaction. MALDI and ESI MS features of $Au_{25-x}Ag_x(SR)_{18}$ (x=1-20) (formed through the inter-cluster reaction route where $Ag_{44}(SR)_{30}$ was the Ag source and not Ag(I) salts; no external reducing agents were used) in positive ion mode were of very low intensity and low signal to noise ratio compared to those observed in the negative ion mode. This indicates that these clusters are also anionic. This also indicates that Ag inclusion through this reaction has not changed the free electron count and the charge state of the resultant bimetallic cluster, as in the case of the clusters obtained through co-reduction methods. Based on the above discussion, it can

thereby be concluded that both the inter-cluster reaction and co-reduction routes incorporate Ag into $Au_{25}(SR)_{18}$ as Ag(0). According to the suggested mechanism depicted in the Schemes 1 and 2, replacement of the Au-SR with Ag-SR would not change the overall charge state and the free electron count in the alloy clusters as there are only rearrangement of bonds involved after the nucleophilic attack and no reduction of Ag^+ or Ag-SR is required. Thus it is likely that in the initial stages of doping, Ag and Ag-SR substituents are more likely to be present on the staples than in the core. Once the staples are opened, substitution of core atoms would become more facile. However, crystal structure data are needed to unambiguously confirm this.

References:

(1) Enkovaara, J.; et al. J. Phys.: Condens. Matter 2010, 22, 253202.
(2) Perdew, J. P.; Burke, K. *Phys. Rev. Lett.* **1996**, *77*, 3865.
(3) Larsen, A. H.; Vanin, M.; Mortensen, J. J.; Thygesen, K. S.; Jacobsen, K. W. *Phys. Rev. B* **2009**, *80*, 195112.
(4) (a) Heaven, M. W.; Dass, A.; White, P. S.; Holt, K. M.; Murray, R. W. *J. Am. Chem. Soc.* **2008**, *130*, 3754. (b) Akola, J.; Walter, M.; Whetten, R. L.; Häkkinen, H.; Grönbeck, H. *J. Am. Chem. Soc.* **2008**, *130*, 3756. (c) Zhu, M.; Aikens, C. M.; Hollander, F. J.; Schatz, G. C.; Jin, R. *J. Am. Chem. Soc.* **2008**, *130*, 5883.
(5) Desireddy, A.; Conn, B. E.; Guo, J.; Yoon, B.; Barnett, R. N.; Monahan, B. M.; Kirschbaum, K.; Griffith, W. P.; Whetten, R. L.; Landman, U.; Bigioni, T. P. *Nature* **2013**, *501*, 399.
(6) Hanwell, M.; Curtis, D.; Lonie, D.; Vandermeersch, T.; Zurek, E.; Hutchison, G. *J. Cheminf.* **2012**, *4*, 1.
(7) Humphrey, W.; Dalke, A.; Schulten, K. J. *Mol. Graphics* **1996**, *14*, 33.
(8) (a) Parker, J. F.; Fields-Zinna, C. A.; Murray, R. W *Acc. Chem. Res.* **2010**, *43*, 1289. (b) Angel, L. A.; Majors, L. T.; Dharmaratne, A. C.; Dass, A. *ACS Nano* **2010**, *4*, 4691.
(9) Wu, Z.; Jin, R. *Nano Lett.* **2010,** *10*, 2568–2573.
(10) (a) Zhu, M.; Eckenhoff, W. T.; Pintauer, T.; Jin, R.*J. Phys. Chem. C* **2008**, *112*,14221. (b) Antonello, S.; Perera, N. V.; Ruzzi, M.; Gascón, J. A.; Maran, F. *J. Am. Chem. Soc.* **2013**, *135*, 15585. (c) Zhu, M.; Aikens, C. M.; Henrich, M. P.; Gupta, R.; Qian, H.; Schatz, G. C.; Jin, R.*J. Am. Chem. Soc.* **2009**, *131*, 2490–2492.(d) Negishi, Y.; Chaki, N. K.; Shichibu, Y.; Whetten, R. L.; Tsukuda, T.*J. Am. Chem. Soc.* **2007**, *129*, 11322. (e) Ghosh, A.; Hassinen, J.; Pulkkinen, P.; Tenhu, H.; Ras, R. H. A.; Pradeep T. *Anal. Chem.* **2014**, *86*, 12185.
(11) (a) Kumara, C.; Aikens, C. M.; Dass, A. *J. Phys. Chem. Lett.* **2014**, *5*, 461. (b) Yamazoe, S.; Kurashige, W.; Nobusada, K.; Negishi, Y.; Tsukuda, T. *J. Phys. Chem. C* **2014**, *118*, 25284. (c) Guidez, E. B.; Mäkinen, V.; Häkkinen, H.; Aikens, C. M. *J. Phys. Chem. C* **2012**, *116*, 20617.
(12) Yao, C.; Chen, J.; Li, M.-B.; Liu, L.; Yang, J.; Wu, Z. *Nano Lett.* **2015**, *15*, 1281.